Defects and Defect Clusters in Compound Semiconductors

by

Brandon McKeon

A Dissertation Presented in Partial Fulfillment
of the Requirements for the Degree
Doctor of Philosophy

Approved April 2020 by the
Graduate Supervisory Committee:

David J. Smith, Co-Chair
Martha R. McCartney, Co-Chair
Jingyue Liu
Yong-Hang Zhang

ARIZONA STATE UNIVERSITY

May 2020

ABSTRACT

Extended crystal defects often play a critical role in determining semiconductor device performance. This dissertation describes the application of transmission electron microscopy (TEM) and aberration-corrected scanning TEM (AC-STEM) to study defect clusters and the atomic-scale structure of defects in compound semiconductors.

An extensive effort was made to identify specific locations of crystal defects in epitaxial CdTe that might contribute to degraded light-conversion efficiency. Electroluminescence (EL) mapping and the creation of surface etch pits through chemical treatment were combined in attempts to identify specific structural defects for subsequent TEM examination. Observations of these specimens revealed only surface etch pits, without any visible indication of extended defects near their base. While chemical etch pits could be helpful for precisely locating extended defects that intersect with the treated surface, this study concluded that surface roughness surrounding etch pits would likely mitigate against their usefulness.

Defect locations in GaAs solar-cell devices were identified using combinations of EL, photoluminescence, and Raman scattering, and then studied more closely using TEM. Observations showed that device degradation was invariably associated with a cluster of extended defects, rather than a single defect, as previously assumed. AC-STEM observations revealed that individual defects within each cluster consisted primarily of intrinsic stacking faults terminated by 30° and 90° partial dislocations, although other defect structures were also identified. Lomer dislocations were identified near locations where two lines of strain contrast intersected in a large cluster, and a comparatively

shallow cluster, largely constrained to the GaAs emitter layer, contained 60° perfect dislocations associated with localized strain contrast.

In another study, misfit dislocations at II-VI/III-V heterovalent interfaces were investigated and characterized using AC-STEM. Misfit strain at ZnTe/GaAs interfaces, which have relatively high lattice mismatch (7.38%), was relieved primarily through Lomer dislocations, while ZnTe/InP interfaces, with only 3.85% lattice mismatch, were relaxed by a mixture of 60° perfect dislocations, 30° partial dislocations, and Lomer dislocations. These results were consistent with the previous findings that misfit strain was relaxed primarily through 60° perfect dislocations that had either dissociated into partial dislocations or interacted to form Lomer dislocations as the amount of misfit strain increased.

To Jerika

ACKNOWLEDGMENTS

I would like to sincerely thank everyone who has contributed, in any way, to the realization of this work. Above all, I wish to express my deepest gratitude to my research advisor and mentor, Regents' Professor David J. Smith, for providing direction along my path and encouragement to see it through. His dedication, patience, and good-natured humor taught me more than just how to be a good scientist. He showed me what it means to be passionate about one's work, and to be tireless in achieving one's goals.

I am also very grateful to Professor Martha R. McCartney for her advice and support. I want to thank Professors Jingyue Liu and Yong-Hang Zhang for serving as members of my supervisory committee and for their time and suggestions.

I appreciate the staff members as well as the use of facilities in the John M. Cowley Center for High Resolution Electron Microscopy at Arizona State University. I give special thanks to Karl Weiss, Kenneth Mossman, and Manuel R. Gutierrez for their training and technical assistance. Financial support by Army Research Office (Grant #W911NF-16-1-0263) is gratefully acknowledged.

I am also grateful for collaborations with Dr. Q. Chen and Dr. Yong Zhang of University of North Carolina at Charlotte, and Dr. Xinyu Liu and Prof. Jacek K. Furdyna of University of Notre Dame.

Particular thanks go to my fellow research group members: Dr. Jing Lu, Dr. Thomas McConkie, Dr. HsinWei Wu, Dr. Majid Vaghayenegar, Dr. Brian Tracy, Dr. Sirong Lu, Allison Boley, Scott Sherman, Abhinandan Gangopadhyay, and Prudhvi Peri. I thank them for sharing with me their knowledge, experience, time, and above all, their friendship.

Last, but certainly not least, I want to express my most heartfelt gratitude to my parents, grandparents, and wife. Without their support and unconditional love I would not be who I am today or have achieved all that I have.

TABLE OF CONTENTS

Page

LIST OF FIGURES ix

CHAPTER

1 INTRODUCTION 1

1.1 Band Structure 2

1.2 Applications in Optoelectronics 6

1.2.1 Photodiodes (PDs)...6

1.2.2 Light-Emitting Diodes (LEDs)..................................8

1.3 Defects in Optoelectronic Materials 9

1.3.1 Crystal Defects 10

1.3.2 Dislocations...13

1.3.3 Stacking Faults 14

1.3.4 Grain Boundaries 15

1.3.5 Misfit Dislocations...17

1.4 Overview of Dissertation..18

References..20

2 EXPERIMENTAL METHODS 21

2.1 Characterization Techniques 21

2.1.1 Chemical Etching 21

2.1.2 Electroluminescence (EL) Imaging.........................22

2.1.3 Scanning Electron Microscopy (SEM) 24

2.1.4 Transmission Electron Microscopy (TEM) 26

CHAPTER Page

2.2 Sample Preparation....29

2.2.1 Wedge Polishing....31

2.2.2 Focused Ion-Beam (FIB)....31

References....33

3 ETCH PITS IN CdTe EPILAYER....35

3.1 Introduction....35

3.2 Experimental Details....36

3.3 Results and Discussion....38

3.4 Conclusions....42

References....44

4 STRUCTURAL DEFECTS IN GaAs SOLAR CELLS....45

4.1 Introduction....45

4.2 Experimental Details....46

4.3 TEM Observations....50

4.4 Discussion and Conclusions....59

References....61

5 ATOMIC STRUCTURE OF INTERFACIAL MISFIT DISLOCATIONS IN II-VI/III-V HETEROSTRUCTURES....62

5.1 Introduction....63

5.2 Experimental Details....65

5.3 Sample Preparation Artefacts....67

5.4 Interfacial 60° Dislocations....69

CHAPTER Page

5.5 Lomer Dislocations 74

5.6 Discussion & Conclusions 77

References 79

6 SUMMARY AND POSSIBLE FUTURE WORK 82

6.1 Summary 82

6.2 Possible Future Work 85

References 87

REFERENCES 88

LIST OF FIGURES

Figure		Page
1.1	Optoelectronics Market Snapshot	1
1.2	Diagram of Kronig-Penney Model	4
1.3	Graphical Solution to the Kronig-Penney Model	5
1.4	Diagram of *p-n* Junction	7
1.5	Comparison of GaAs and Ge Band Structures	9
1.6	Diagram of Energy Bands vs. Lattice Constant	11
1.7	Possible Energy Transitions Within the Band Gap	12
1.8	Perfect Edge Dislocation Diagram	13
1.9	Examples of Stacking Faults in GaAs	15
1.10	Low-Angle Grain Boundary Diagram	16
1.11	Misfit Dislocation Diagram	17
2.1	Diagram of Carrier Recombination Through Donor Levels	23
2.2	SEM Schematic	25
2.3	TEM Schematic	27
3.1	SEM Image of Chemical Etch Pits in CdTe Epilayer	37
3.2	PL Map of Defects in CdTe Epilayer	37
3.3	TEM Cross Section Image of a Large Etch Pit	39
3.4	TEM Image of a Large Etch Pit at Higher Magnification	39
3.5	TEM Cross Section Image of a Small Etch Pit	40
3.6	TEM Image of a Small Etch Pit at Higher Magnification	41
4.1	Diagram of the GaAs Solar-Cell Device	47

Figure | Page

4.2 PL Map, Raman Spectra, and I-V Curves 48

4.3 EL Map and Optical Image of Defect Locations in GaAs Solar Cell 49

4.4 TEM Images of a Defect Cluster 50

4.5 HAADF Image and Model of 30° and 90° Partial Dislocations 51

4.6 HAADF Image and Model of Two 30° Partial Dislocations 51

4.7 TEM Image of Extensive Defect Cluster 53

4.8 LABF STEM Image of 30° Partial Dislocation 54

4.9 LABF STEM Image for Intensity Profiles 56

4.10 Inverted Integrated Intensity Profile of GaAs Atomic Dumbbells 56

4.11 LABF STEM Images of a Lomer Dislocation 57

4.12 TEM Image of Confined Defect Cluster 58

4.13 HAADF STEM Image of 60° Perfect Dislocation 59

5.1 Schematic of Band-Gap Energy Vs. Lattice Constant of Common Semiconductor Materials 64

5.2 TEM Images of FIB-Prepared ZnTe/GaAs and ZnTe/InP Interfaces 67

5.3 Higher Magnification TEM Image of FIB-Prepared ZnTe/InP Interface 68

5.4 TEM Image of Wedge-Polished ZnTe/GaAs Interface 69

5.5 LABF Image of 60° Perfect Dislocation at ZnTe/InP (100) Interface 70

5.6 Integrated Intensity Profiles Across ZnTe/InP (100) Interface 71

5.7 LABF Image of 60° Perfect Dislocation at ZnTe/GaAs (100) Interface............72

5.8 LABF Images of 60° Perfect and 30° Partial Dislocations at ZnTe/InAs (100) Interface 73

Figure | Page

5.9 LABF Image and Integrated Intensity Profiles of 90° Lomer Dislocation at ZnTe/InP (100) Interface 74

5.10 Proposed Dislocation Core Structure of 90° Lomer Dislocation at ZnTe/InP (100) Interface 75

5.11 LABF Image and Integrated Intensity Profile of Conventional Shuffle Type Lomer Dislocation at ZnTe/GaAs (100) Interface 76

5.12 LABF Image and Integrated Intensity Profile of Disordered Lomer Dislocation at ZnTe/GaAs (100) Interface 77

CHAPTER 1

INTRODUCTION

Optoelectronic devices are an integral part of daily life for billions of people all over the world. Common optoelectronic devices include: light-emitting diodes (LEDs) found in computer monitors, cell phones, and as indicator lights; laser diodes (LDs) used in laser pointers, printers, barcode readers and CD or Blu-ray players; and photodiodes (PDs) such as solar cells and light sensors used in televisions and cameras.[1] Figure 1.1 gives a snapshot of the global optoelectronics market in 2017, showing the monetary value of several types of these devices.

The electronic properties of any specific device are basically determined by the materials properties. For example, the compound semiconductors CdTe and GaAs have direct band gaps of about 1.48 and 1.42 eV, respectively, making them promising choices for devices such as solar cells.[3,4] However, the crystal defects that are present in materials

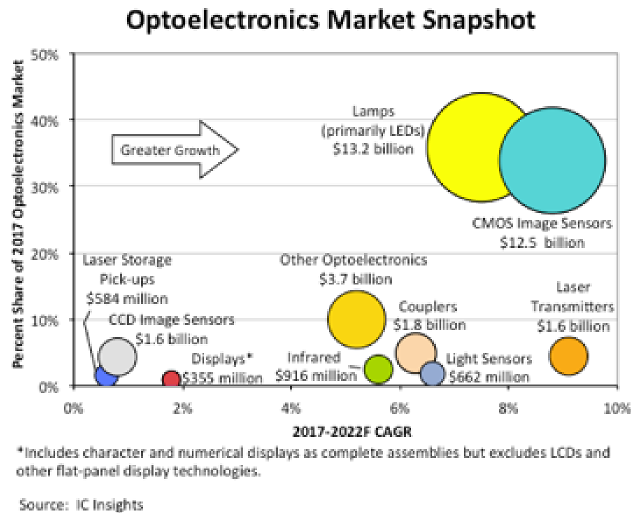

Figure 1.1: Percentage market share of optoelectronic devices and their compound annual growth rate. Device share values are indicated.[2]

often control the device performance just as much or more than the intrinsic material properties.[5,6] In the case of CdTe solar cells, it has been found that polycrystalline thin-film devices with a high density of grain boundaries perform with higher efficiency, after $CdCl_2$ heat treatment, than single crystal cells.[3] This beneficial effect is attributed to the high concentration of Cl doping at the grain boundaries, which causes formation of *p-n-p* junctions across grain boundaries from one grain to adjacent grains, and also provides a conduction path along grain boundaries for photon-generated charge carriers to be separated.[3]

The ever-increasing demand for optoelectronic devices with greater efficiency and longer lifetimes has stimulated investigation of novel materials. Despite this ongoing effort, comprehensive understanding of specific defects and their impact on optoelectronic properties, as well as the resulting behavior of particular devices, is generally lacking. The research in this dissertation focuses on atomic-scale structure and composition of defects in III-V compound semiconductors, and explores how these defect structures correlate with device performance.

1.1 Band Structure

Materials are composed of atoms which consist of a nucleus surrounded by electrons. While the atomic nuclei basically determine the material's underlying physical structure, they are relatively immobile in a solid and do not contribute to the material's electronic properties. Therefore, to understand fully the role of semiconductors in modern electronic devices, it is first necessary to determine the behavior of electrons in these materials.

The modern view of the atomic structure of a material considers the electron within the framework of quantum mechanics. Calculating the energy levels and wavefunctions of many electrons within the complex potential distribution of an actual material is a challenging problem that requires substantial computing power and sophisticated algorithms. While these calculations are essential for specific materials systems, a general conceptual understanding can be obtained by considering simplified models, beginning with a model for an electron in free space.

The time-independent Schrödinger equation for an electron in free space can be represented by the expression

$$\left(\frac{-\hbar^2}{2m}\nabla^2 + V_0\right)\psi(r) = E\psi(r) \tag{1.1}$$

where m is the mass of the electron, ∇^2 is the Laplacian operator, V_0 is a constant potential, E is the energy, and $\psi(r)$ is the spatial component of the wavefunction. Solving this equation results in solutions of the form

$$\psi(r) = \exp(\pm i\boldsymbol{k} \cdot r) \tag{1.2}$$

where $\boldsymbol{k}$ is the wavenumber. All values of $\boldsymbol{k}$ are allowed and each corresponds to a particular solution to the Schrödinger equation. The electron's energy and momentum are then given by

$$E = \frac{\hbar^2 k^2}{2m} + V_0 \text{ and } \boldsymbol{p} = \hbar\boldsymbol{k}. \tag{1.3}$$

The electrons in a semiconductor are not free, but are instead influenced by a periodic array of atomic nuclei. As a first approximation, known as the Kronig-Penney model, these nuclei can be modeled as an infinite, periodic array of potential wells, as shown in figure 1.2. In order to simplify the mathematics, the bases of the wells are

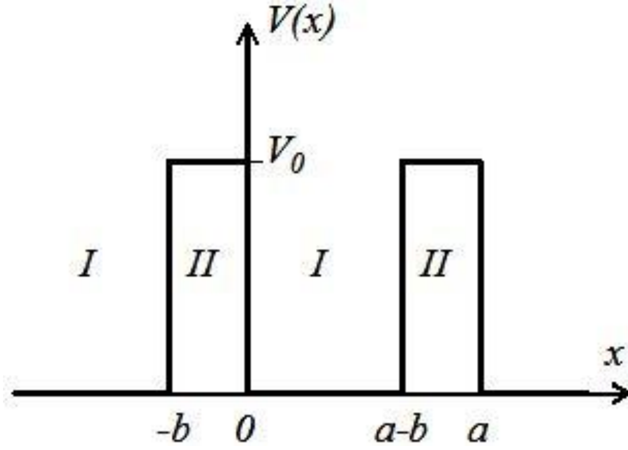

Figure 1.2: Representation of a portion of the Kronig-Penney model.[5]

defined to be at zero potential while the heights of the barriers are defined by V_0. The width of the barriers is *b*, and the well width is *a-b*, so that the period of the potential wells is *a*. Using this well model, and solving the Schrödinger equation results in solutions with energy *E* and wavenumber *k* that satisfy the equation[5]

$$\cos(ka) = \cos(qb)\cosh\big(|\kappa|(a-b)\big) - \frac{q^2-\kappa^2}{2q\kappa}\sin(qb)\sinh\big(|\kappa|(a-b)\big) \quad (1.4)$$

where

$$\kappa = \frac{\sqrt{2m(E-V_0)}}{\hbar} \text{ and } q = \frac{\sqrt{2mE}}{\hbar}. \quad (1.5)$$

There are no restrictions on the possible values of *k*, but there are certain energy ranges that are not accessible, as can be seen in figure 1.3, which shows an electron energy spectrum for a specific choice of parameters in the Kronig-Penney model. This spectrum separates the allowed energies into energy bands or shells which play a key role in determining the electrical properties of the material.

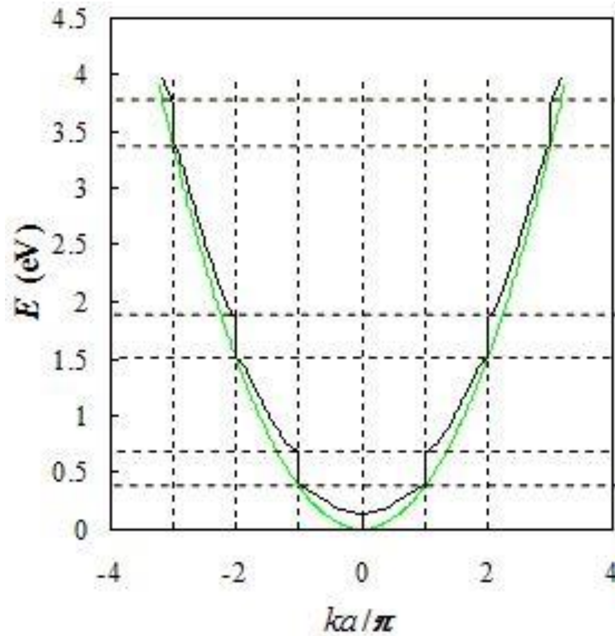

Figure 1.3: Solution to the Kronig-Penney model when a = 1 nm and the product $V_0 \cdot b$ = 0.2 nm-eV. Solution for a free electron is shown in grey.[5]

If all of the energy states in a band are not filled, then the energy difference between filled and empty states is negligible, and very little energy is required to excite electrons into higher energy states. In other words, the electrons are highly mobile, so that materials with partially filled bands are good conductors. Conversely, when the highest energy state in a band is filled, this highest filled state and the lowest available empty state are separated by a finite band gap. Thus, relatively more energy is required to excite electrons into unfilled states. These types of materials are considered as either semiconductors or insulators, depending on the size of the band gap. While the cut-off band-gap energy between semiconductors and insulators is ill-defined, it is generally considered that materials with a band gap below about 4 eV are semiconductors, while those with greater band-gap energies are commonly classified as insulators.

1.2 Applications in Optoelectronics

Optoelectronic devices convert light energy to electrical energy or *vice versa*. For example, an LED uses the energy from an electrical signal to emit photons and a solar cell uses the energy from photons to produce electrical current. While there are many different processes for these types of energy conversion, they are generally quantum mechanical in nature and are based on the generation or recombination of mobile charge carriers across the band gap of the active material. The motion and interaction of the mobile charge carriers can often be predicted for theoretical devices, and the resulting optoelectronic properties can be calculated. However, real devices are composed of materials that contain structural defects such as dislocations and stacking faults. These defects can strongly interact with the charge carriers and thus dramatically alter the intended functionality of the device.

1.2.1 Photodiodes (PDs)

A photodiode is an optoelectronic device that makes use of the photovoltaic (PV) effect. The PV effect is the direct conversion of energy from light into an electric current. There are two processes necessary in order for this conversion to take place.[7] First, photons are absorbed by the semiconductor, transferring energy to electrons in the material, possibly causing their ejection and the generation of electron-hole pairs. The second step is separation of these charge carriers before they recombine. This charge separation is usually achieved by using a *p-n* junction, although other mechanisms exist.

Efficient PV conversion depends strongly on material properties. In order for the light energy to be converted into current, the incoming photon must first be absorbed by the material by exciting a bound electron into a higher energy state. In a metal, which has

a continuous energy band, the electrons are easily excited but then relax too quickly for any significant PV effect to occur. In an insulator, the band gap between the valence band (VB) and the conduction band (CB) is too large, so that the large majority of incoming solar photons do not have sufficient energy to excite valence electrons to higher energy levels.

Semiconductors have band-gap energies that are similar to the photon energies that correspond to visible light. Furthermore, the band gap of semiconductors is highly sensitive to material composition. Therefore, adding impurities or controlling the relative concentration of different elements in a compound material allow for manipulation of the band gap in order to match the desired energy ranges. These characteristics make many semiconductor compounds ideal for use in photodiodes.

Once an electron-hole pair has been created through photon absorption, the charge carriers need to be separated so that an electrical current can be extracted. When there is an applied or built-in electric field in the active absorption region, that field will move the electrons and holes apart from one another. Figure 1.4 illustrates how this is

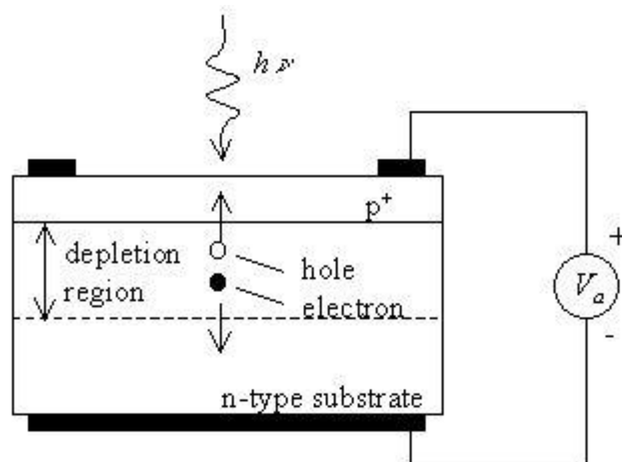

Figure 1.4: Motion of electrons and holes after photon absorption under the influence of the built-in field created by a *p-n* junction.[5]

accomplished with a *p-n* junction. When a photon is absorbed near the depletion region and creates an electron-hole pair, the built-in field created by the junction forces electrons toward the *n*-type layer and holes toward the *p*-type layer, effectively separating them before they can recombine.[5] When engineering a photodetector, it is important to match the absorption depth of the light to the active region of the device because electron-hole pairs created away from the region of the electric field are likely to recombine before being separated.[7]

1.2.2 Light-Emitting Diodes (LEDs)

A light-emitting diode works opposite to that of a photodetector. An LED uses electrical bias to move excess electrons in the CB of a material toward excess holes in its VB, thus stimulating recombination. In the presence of a *p-n* junction, an external bias must be applied to force electrons in the *n*-type material and holes in the *p*-type material to move toward the depletion region where they can recombine.[5]

Recombination can take place through both radiative and non-radiative processes. A radiative process results in the creation of a photon with energy equal to the difference between the final and initial energy states of the electron going through recombination. In the case of non-radiative recombination, the energy released by the electron is converted into one or more phonons. High minority-carrier densities tend to encourage radiative recombination processes over non-radiative processes.[5] Producing a photon during recombination is also more likely for direct band-gap materials, such as GaAs, than it is for indirect band-gap materials such as Si or Ge. Figure 1.5 is a graphical representation of the band gap for GaAs and Ge. The transition from the lowest energy state of the CB of GaAs to the highest energy state in the VB requires only a change in energy, which

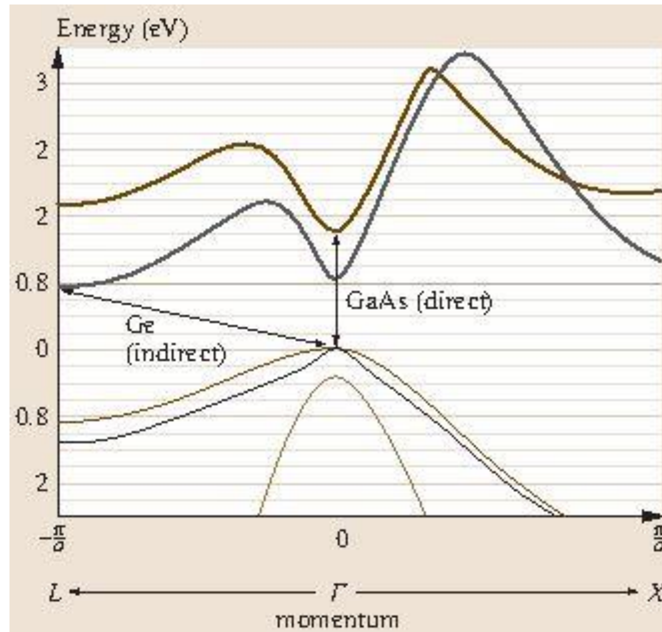

Figure 1.5: Comparison of band structure of GaAs and Ge.[7]

can be easily accommodated by creation of a photon. In an indirect band-gap material such as Ge, the transition from the lowest CB energy state to the highest available state in the VB requires a change in both energy and momentum. As photons carry away negligible amounts of momentum compared with the momentum of electrons and holes, the recombination of an electron and hole in an indirect band-gap material would only produce a photon if it also produces a phonon simultaneously. Thus, direct band-gap materials make far more efficient LED devices.[7]

1.3 Defects in Optoelectronic Materials

Crystal defects usually have a profound effect on the physical and electrical properties of materials. Many types of defects, including point defects, dislocations, and domain boundaries, alter the photoelectric properties of a material by increasing or decreasing the band-gap energy, introducing acceptor or donor energy states within the

band gap, or by creating locations in the material where charge carriers are trapped and recombine rather than contributing to the generated current.[3,5,6,7]

There are many theories concerning how a specific extended defect may influence the performance of an optoelectronic device. For example, strain introduced into a material by the presence of dislocations can cause local band-bending or even introduce new accessible energy levels within the band gap.[6] Partial dislocations with different core structures, separated by a stacking fault, would cause spatial distortions in the energy band gap and potentially act to separate electron-hole pairs.[3] Stacking faults could be considered as a local change in the crystal structure, which would cause that region to have different band structure from that of the surrounding area, potentially behaving like a quantum well.[3] Furthermore, grain boundaries decorated with dopants or impurities could preferentially attract either electrons or holes and act as pathways for charge carriers.[3] Very little research has so far been done to determine exactly how specific extended defects affect the performance of real devices.

1.3.1 Crystal Defects

The electronic properties of a material are primarily governed by the behavior of electrons, which are fundamentally influenced by the structural arrangement of atomic nuclei in the material, particularly in the case of crystalline semiconductor devices. The periodic arrangement of atomic nuclei in a crystal provides the underlying potential that results in the formation of electron energy bands separated by gaps, as previously shown using the Kronig-Penney model. Figure 1.6 shows a theoretical simulation of the allowed energies in crystalline carbon (diamond) as a function of the lattice parameter, i.e., the period of the crystal lattice.[5] As the spacing between atoms changes, the availability of

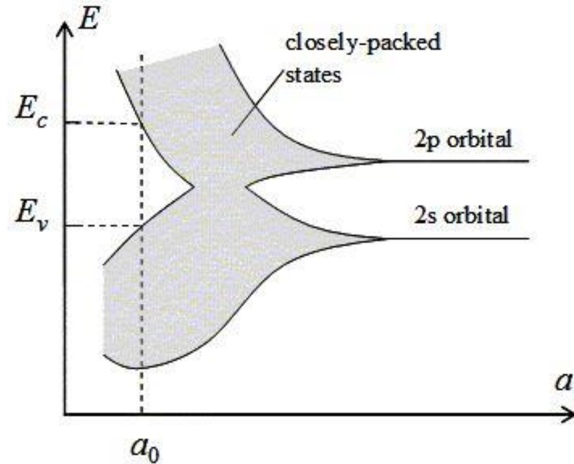

Figure 1.6: Energy bands as a function of lattice constant (*a*) for diamond.[5]

electron energy states also changes. At sufficiently large distances between atoms, electrons are effectively isolated to a single atomic nucleus and the only available electron energy states are those allowed for a single atom. When atoms are arranged more closely together, electrons can be influenced by more than one atomic nucleus and the discrete electron energy states of a single atom become energy bands with a range of available electron energy states.

Defects in the crystal lattice directly impact the performance and properties of semiconductor materials.[6] Common crystal defects found in III-V optoelectronic materials include point defects, such as atomic substitutions or interstitial atoms, as well as extended defects, like dislocations, stacking faults, and grain boundaries.[8] Research concerning the effect of these types of defects is ongoing, and the role of point defects in semiconductor devices, especially optoelectronic devices, is considered to be relatively well understood. Incorporating extrinsic atoms, or dopants, into a crystal introduces donor or acceptor energy levels into the energy band gap.[6] Figure 1.7 illustrates some possible transitions that a charge carrier could make when donor and acceptor dopants are

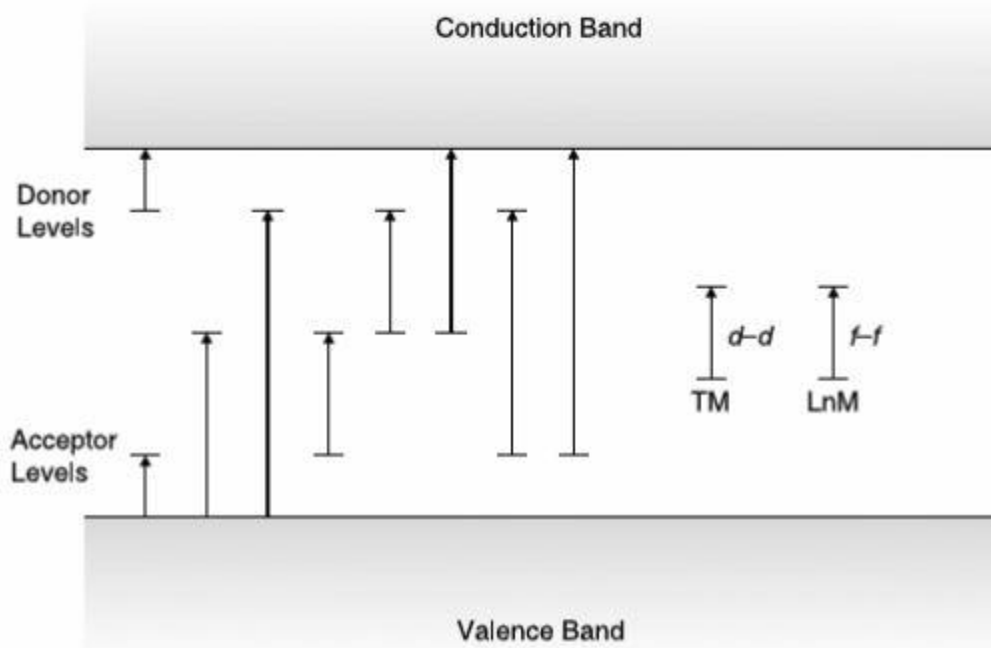

Figure 1.7: Possible energy transitions within the band gap of a material when point defects are present. When transition-metal (TM) ions are present, the transitions are between *d* orbitals. Likewise, lanthanide (LnM) ions cause transitions between *f* orbitals.[6]

present. This alteration of behavior due to dopants allows for devices to be engineered with properties that are dependent on specific energy levels, but also implies that unwanted dopants, or impurities, also have the potential to dramatically alter the device properties.

Extended crystal defects are well documented, but they are not as well understood as point defects with regard to their impact on optoelectronic device behavior. Extended defects are generally categorized based on their dimensionality. Dislocations are one-dimensional, or line, defects. Two-dimensional, or planar, defects include stacking faults, grain boundaries, twin boundaries, and anti-phase boundaries. Extended defects alter the local atomic structure of the material and can introduce stresses and strain into the crystal lattice.[6,8] In general, extended defects degrade optoelectronic devices and limit their

performance, but there are examples where the opposite is true.[3,8] For example, as mentioned previously, Cl-rich grain boundaries in thin-film polycrystalline CdTe solar cells provide pathways for charge carriers to be separated much more quickly.[3]

1.3.2 Dislocations

A dislocation can be considered as a disturbance in the periodic ordering of atoms in a crystal.[6,8] Dislocations never terminate inside the bulk of a material, but rather end either on the surface of the material, at another dislocation, or else they loop around on themselves.[6] The bonds between nearby atoms are strained and distorted along the line of the dislocation. The distortion in the crystal lattice caused by a dislocation is commonly characterized by the Burgers vector, **b**, and the formation energy of a dislocation is proportional to $\mathbf{b}^2$.[8] While the Burgers vector of a dislocation could, in principle, make any angle to the dislocation line, all dislocations can be considered as either edge dislocations, which are characterized by having Burgers vectors perpendicular to the dislocation line, screw dislocations, where the Burgers vector and the dislocation line are parallel, or else as some linear combination of the two. Figure 1.8 is a representation of a

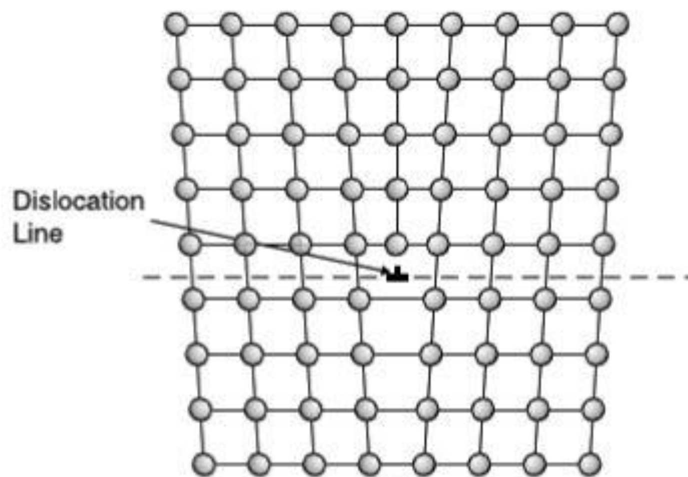

Figure 1.8: Perfect edge dislocation viewed in end-on projection.[6]

perfect edge dislocation in a monatomic crystal with the dislocation line normal to the plane of the page and the Burgers vector (not shown) parallel to the plane of the page and pointing to the left. Due to crystal symmetries and different bonding strengths, it is common to find that specific types of dislocations form more frequently in certain crystal structures. For example, many optoelectronic devices are based on face-centered-cubic materials that tend to exhibit mixed dislocations with the Burgers vector inclined at 60° to the dislocation line.[8]

Due to the strain fields associated with dislocations, other defects such as precipitates, dopants, and impurities tend to be attracted to dislocations and cluster near and around them. This effect is commonly called dislocation decoration. The crystal disruption occurring around dislocations also increases the probability of atomic motion. Thus, atomic diffusion near a dislocation is generally much greater than in the surrounding area.[6]

1.3.3 Stacking Faults

A perfect dislocation can reduce its strain energy by dissociating into two partial dislocations and a stacking fault. In cubic semiconductors, an intrinsic stacking fault is created when one {111}-type plane is removed from what would otherwise be a perfect stacking sequence. In other words, the stacking sequence of an intrinsic stacking fault is ...AaBbCcBbCc... On the other hand, when an extra plane is inserted into the perfect crystal, an extrinsic stacking fault, with stacking sequence ...AaBbCcB*b*AaBbCc... is formed.[8] Figure 1.9 shows examples of both intrinsic and extrinsic stacking faults in GaAs.[8]

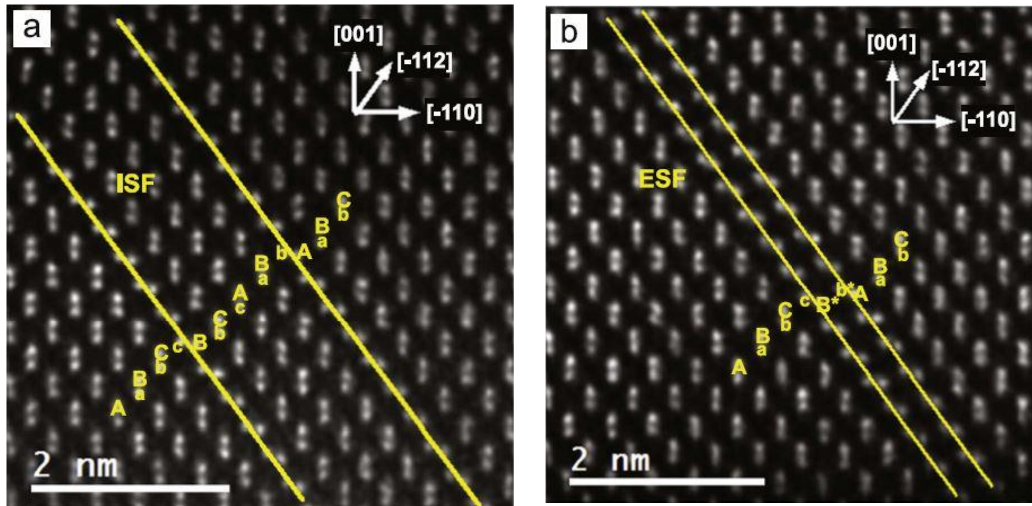

Figure 1.9: Stacking faults in GaAs. a) Two intrinsic stacking faults, and b) One extrinsic stacking fault. Stacking fault planes and sequences are indicated.[8]

1.3.4 Grain Boundaries

Many devices are created with polycrystalline materials, or materials that are comprised of many different crystal orientations or grains, rather than from single crystals. The interfaces between these grains are called grain boundaries (GBs). Figure 1.10 is a schematic representation of a low-angle GB where the two grains are slightly misaligned by a small crystal tilt. It is also possible for two grains to be misaligned by a twist, or any combination of the two. The GB between two grains can often be considered as equivalent to an array of dislocations, separated by a distance, d, that remove the misfit between the two parts.[6]

Grain boundaries are locations within a crystal that have a relatively high degree of disorder. Thus, GBs tend to attract other defects and also improve diffusion rates of dopants and impurities, similar to dislocations.[6]

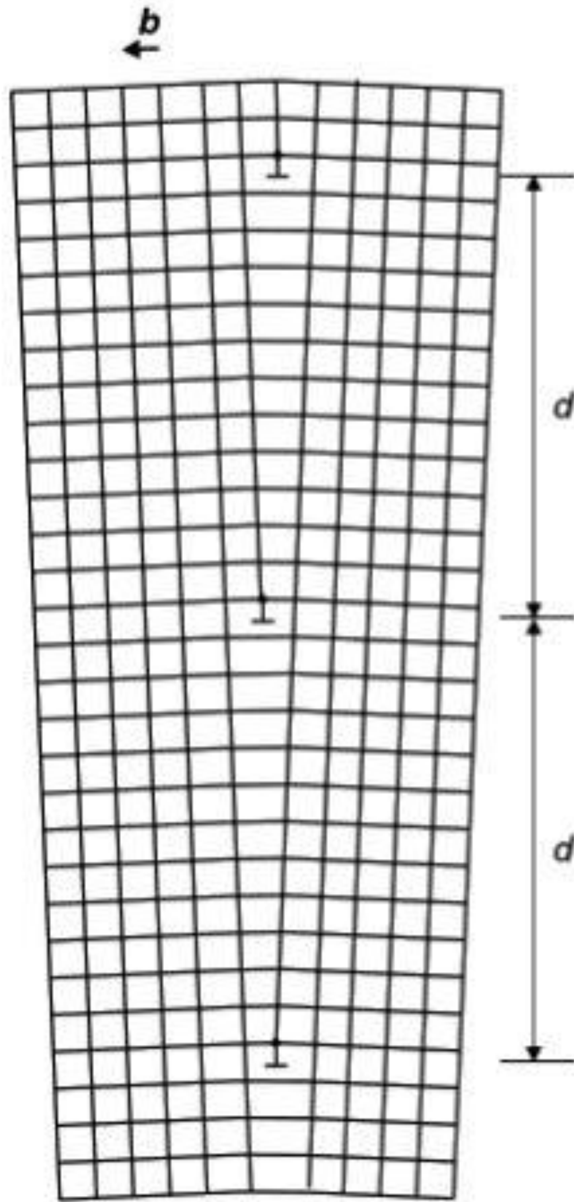

Figure 1.10: Low-angle grain boundary.

1.3.5 Misfit Dislocations

Semiconductor devices are often made up of interfaces between different materials. When a material is grown on top of another material and the lattice parameters of the materials do not match, the atoms in the material being grown attempt to conform to the lattice of the base material, as seen in figure 1.11. This creates a strain field near the interface. When the grown material reaches a critical thickness, dislocations are introduced at the interface that relax the strain, as also shown in figure 1.11. These dislocations are called misfit dislocations.

While the influence of defects, such as stacking faults and misfit dislocations, on structural and chemical properties is often well understood, detailed knowledge about their effect on optical and electronic properties is still generally lacking.

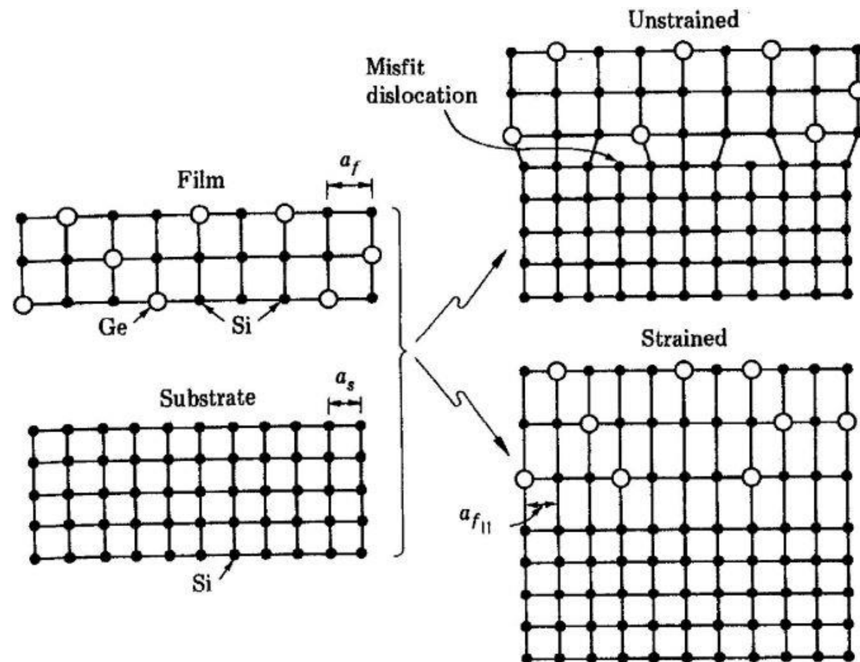

Figure 1.11: Formation of misfit dislocations in a heterostructure to remove misfit strain.[9]

1.4 Overview of Dissertation

The research of this dissertation is directed towards bridging the current knowledge gap between defect characterization and device performance at the atomistic scale. In chapter 2, methods that are used to characterize extended defects are described. These characterization techniques include electroluminescence imaging, transmission electron microscopy (TEM), high-resolution TEM (HRTEM), and scanning TEM (STEM). Sample preparation techniques, as well as various challenges associated with sample preparation and their solutions, are also briefly described.

Chapter 3 outlines the work carried out to identify and characterize individual defects for correlation with localized device performance. The use of dual beam FIB-SEM and TEM to locate defects at the base of etch pits in a CdTe epilayer is described. Challenges that impeded this effort are discussed.

The characterization of extended defects at locations of decreased device performance in GaAs solar-cell devices is detailed in Chapter 4. Locations where the device fails to luminesce under external excitation are found to correspond to the presence of defect clusters. Various defect clusters are compared and their differences discussed. Atomic-scale characterization of individual defects using STEM is also described.

In Chapter 5, misfit dislocations (MDs) in ZnTe/GaAs, ZnTe/InP, and ZnTe/InAs heterostructures are characterized using TEM and STEM. Individual MD core structures are characterized. The relationship between the magnitude of lattice mismatch and the resulting MD core structure is described. Integrated intensity profiles reveal that these

interfaces are not atomically abrupt, and the impact of interfacial chemical intermixing on misfit dislocation atomic structure is discussed.

Chapter 6 provides a summary of important results and conclusions in the dissertation. Possible topics for further investigation are also briefly described.

References

[1] M. Fukuda, "Historical overview and future of optoelectronics reliability for optical fiber communication systems." Microelectronics Reliability **40**, 27-35 (2000).

[2] O-S-D Report, IC Insights, (2017) http://www.icinsights.com/services/osd-report/report-contents/

[3] C. Li, J. Poplawsky, Y. Yan, and S.J. Pennycook, "Understanding individual defects in CdTe thin-film solar cells via STEM: From atomic structure to electrical activity." Materials Science in Semiconductor Processing **65**, 64-76 (2017).

[4] J. S. Blakemore, "Semiconducting and other major properties of gallium arsenide." Journal of Applied Physics **53**, (1982).

[5] B. Van Zeghbroeck, Principles of Semiconductor Devices, ECEE Colorado, 2011.

[6] R. J. D. Tilley, Defects in Solids. John Wiley & Sons, Incorporated, 2008, p. 85.

[7] S. J. Sweeney and J. Mukherjee, (2017) Optoelectronic Devices and Materials. In: Kasap S., Capper P. (eds) Springer Handbook of Electronic and Photonic Materials. Springer Handbooks. Springer, Cham.

[8] Y. A. R. Dasilva, R. Kozak, R. Erni, and M. D. Rossell, "Structural defects in cubic semiconductors characterized by aberration-corrected scanning transmission electron microscopy." Ultramicroscopy **176**, 11-22 (2017).

[9] Cheung, N. (2020, February 13). *Defects Tutorial*. Retrieved from http://www-inst.eecs.berkeley.edu/~ee143/sp06/lectures/Defects_tutorial.pdf

CHAPTER 2

EXPERIMENTAL METHODS

2.1 Characterization Techniques

Locating and identifying defects in semiconductor materials are important steps towards understanding how specific defects can impact the quality of the material and operation of the device in which it is being used. Many characterization techniques are used for this purpose, each with its own capabilities and limitations. Examples of these techniques include photoluminescence (PL), electroluminescence (EL), chemical etching, x-ray diffraction (XRD), transmission electron microscopy (TEM), scanning electron microscopy (SEM), Raman spectroscopy, atomic-force microscopy, and atom-probe tomography. The techniques that were used in this dissertation research are briefly described in the following.

2.1.1 Chemical Etching

Chemical etching of a material is done for several reasons, including locating and counting microstructural defects, primarily dislocations, that terminate at the material's surface.[1] Dislocations can be considered as distortions in the crystalline matrix of the material, which result in the dislocation core being surrounded by a strain field. The strain caused by the presence of the dislocation often results in locally enhanced chemical reactivity.[2] Because the region around the defect reacts differently than the surrounding non-defective area, treating the sample surface with a suitable etchant often results in etch pits that identify the defect location.

Etch pits can sometimes be large enough to be identified with an optical microscope, so that the etching is primarily used for macroscopic evaluation.[1] Smaller

etch pits can be enlarged with continued etching or else characterized using another technique such as scanning electron microscopy. When the defect density exceeds on the order of $10^6 cm^{-2}$, the technique becomes less useful for counting purposes as the resulting etch pits begin to overlap.[1] Although the approach is destructive, it is highly reliable for certain types of semiconductors, it allows for high speed of testing, and it is not very expensive.[1] It has also been shown that the shapes of etch pits can depend on the type and distribution of dopant in the semiconductor, the composition of the etchant, and the orientation of the surface.[3-5] More recent work correlated chemical etching and PL results in an effort to better understand the role of the defects in affecting the performance of optoelectronic devices. It was concluded that the etch pits did not always match the locations of optoelectrically active defects revealed through PL, or *vice versa*.[6]

2.1.2 Electroluminescence (EL) Imaging

Electroluminescence describes the process whereby a material emits photons due to an applied electrical current or in the presence of a strong electric field.[7] The process of creating a photon through electron-hole recombination depends on the crystalline quality, the presence of dopants or impurities, and the material's band structure.[8] In a perfect semiconductor, no available energy states exist within the band gap. Thus, when current is applied, the injected charge carriers recombine through direct band-to-band transitions. When the recombination is radiative, this process results in photon emission with energy corresponding to the specific band gap.[9]

In a real device, the presence of structural defects, dopants, and impurities can introduce energy states within the band gap.[10] These energy states provide opportunities

for recombination with less energy, or they can act as electron traps that delay recombination from taking place.[11-13]

For example, consider a defect associated with a deep donor level as shown in figure 2.1. The defect supplies an extra electron that can combine with a hole in the valence band and produce either a phonon or photon. The defect is now ionized and can

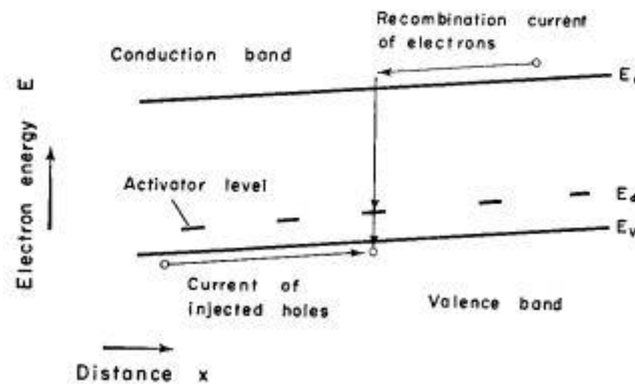

Figure 2.1: Diagram depicting the recombination of injected holes through donor levels in the band gap.[12]

accept an electron from the conduction band with a transition energy that is necessarily less than that required for a band-to-band transition.[12] Thus, in the vicinity of this defect, instead of producing photons with energies equal to the band-gap energy when excited, the material could produce photons with two different energies corresponding to the two intermediate transitions, assuming that both transitions are radiative. On the other hand, if the material contains a defect associated with an acceptor level, electrons in the conduction band can relax into the acceptor level and be excited back into the conduction band through thermal fluctuations. Thus, the defect can act as an electron trap, potentially increasing the lifetime of electron-hole pairs and thereby reducing photon emission.[11,13]

Electroluminescence imaging takes advantage of variations in emission spectra as an approach to identify the locations of localized distortions in the crystalline material. The technique consists of applying current to the device and then observing local variations in light emission across the device surface.[14,15] The light emitted depends on local crystalline defects that alter optical and electrical properties. However, it is often difficult to identify and distinguish between different types of defect in an EL image.[14]

2.1.3 Scanning Electron Microscopy (SEM)

An electron microscope uses a beam of electrons and a column of magnetic or electrostatic lenses to produce images of a sample. In the case of the SEM, electrons are typically accelerated to energies in the range of 0.1 to 30 keV.[16] When the high-energy electrons interact with atoms in the sample, a wide variety of signals, including back scattered electrons, secondary electrons, and characteristic x-rays, are emitted.[16] The electron beam is scanned across the sample, and the resulting signals are collected to create images or spectra of the sample surface.[16]

Figure 2.2 shows a schematic of a standard SEM, and indicates many of the components that are used to form the electron beam and the final image. The electron gun generates and accelerates the electrons to the desired energy.[16] However, the spot produced by the electron gun is normally too large to produce a sharp image, so condenser lenses are used to demagnify the electron source and focus the electrons.[16] The objective lens (not labeled in figure 2.2) is the last lens in the column and focuses the electron probe onto the surface of the sample while also contributing a small amount of demagnification.[17] Scan coils are used to raster the electron beam across the sample. A scan generator controls both the scan coils and the generation of a similar raster on a

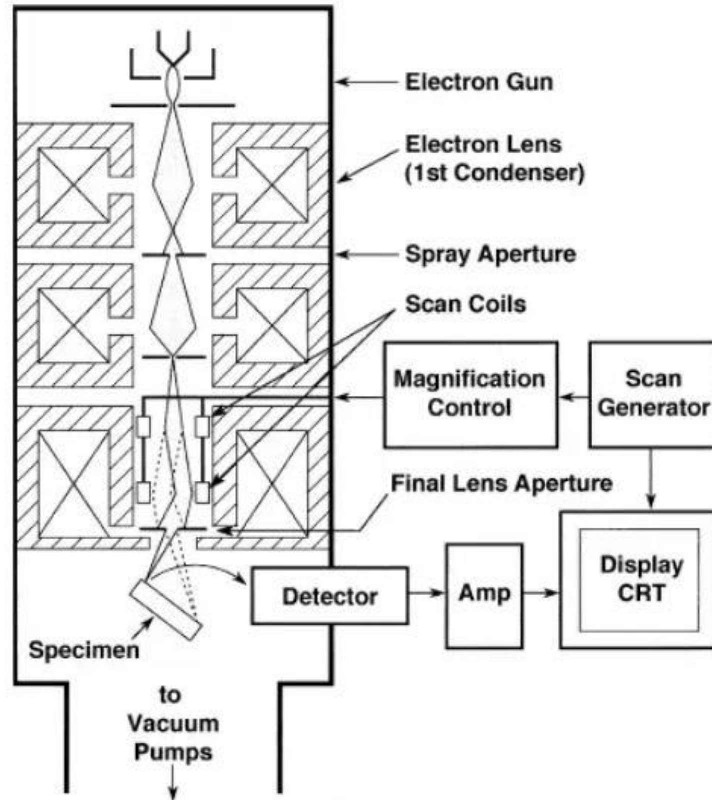

Figure 2.2: Schematic of SEM with major parts labeled.[16]

viewing screen. The final image magnification is given by the ratio of length of the raster on the viewing screen to the corresponding length of the raster across the specimen.[16]

Because the probe diameter is usually on the order of nanometers or less, which is much smaller than the wavelength of visible light (about 380 to 750 nm), the SEM can produce images with much higher magnification and spatial resolution than possible with a standard light microscope. Modern SEMs can routinely achieve resolutions of less than 1 nm with suitably thin samples.[18] However, the probe size only sets a lower limit on the achievable resolution.[19] When the electron beam interacts with the sample, electrons are scattered by atoms in the sample, which results in beam broadening. Depending on the sample composition and thickness, as well as the electron beam energy, the area from

which secondary electrons and back-scattered electrons are collected to form the image may be significantly larger than the incident beam spot.[19]

2.1.4 Transmission Electron Microscopy (TEM)

The TEM is a highly versatile instrument capable of acquiring structural and analytical information over a very wide range of length scales ranging from sub-Ångstrom to several microns.[20] The flexibility and adaptability of the TEM stem from the large number of components. Figure 2.3 identifies many of these components. The electron gun is the source of the electron beam, which is accelerated in stages to high energy, typically 100 to 300 keV in modern TEMs.[21] The system of condenser lenses and apertures, together with the electron gun and accelerator, form the beam that is used to probe the sample. The objective lens is the primary lens used for imaging, and the following transfer lenses produce the final magnified image. All of the lenses in the column are important and participate in formation of the final image, but the aberrations and imperfections of the objective lens are most important since their effects are included in the image, convoluted with the desired specimen information.[22]

In contrast with the typical SEM, relatively high accelerating voltages are used in modern-day TEMs. The high-energy electrons mostly pass through the thinned sample, causing interactions to take place throughout the bulk of the sample rather than mostly at or near the surface. Furthermore, electrons with higher energy also have shorter wavelength, providing the possibility for better spatial resolution. TEM energies range from 30 keV up to 3.0 MeV, but most TEMs are operated between 100 to 300 keV since higher electron energies are liable to result in substantial sample damage.[21]

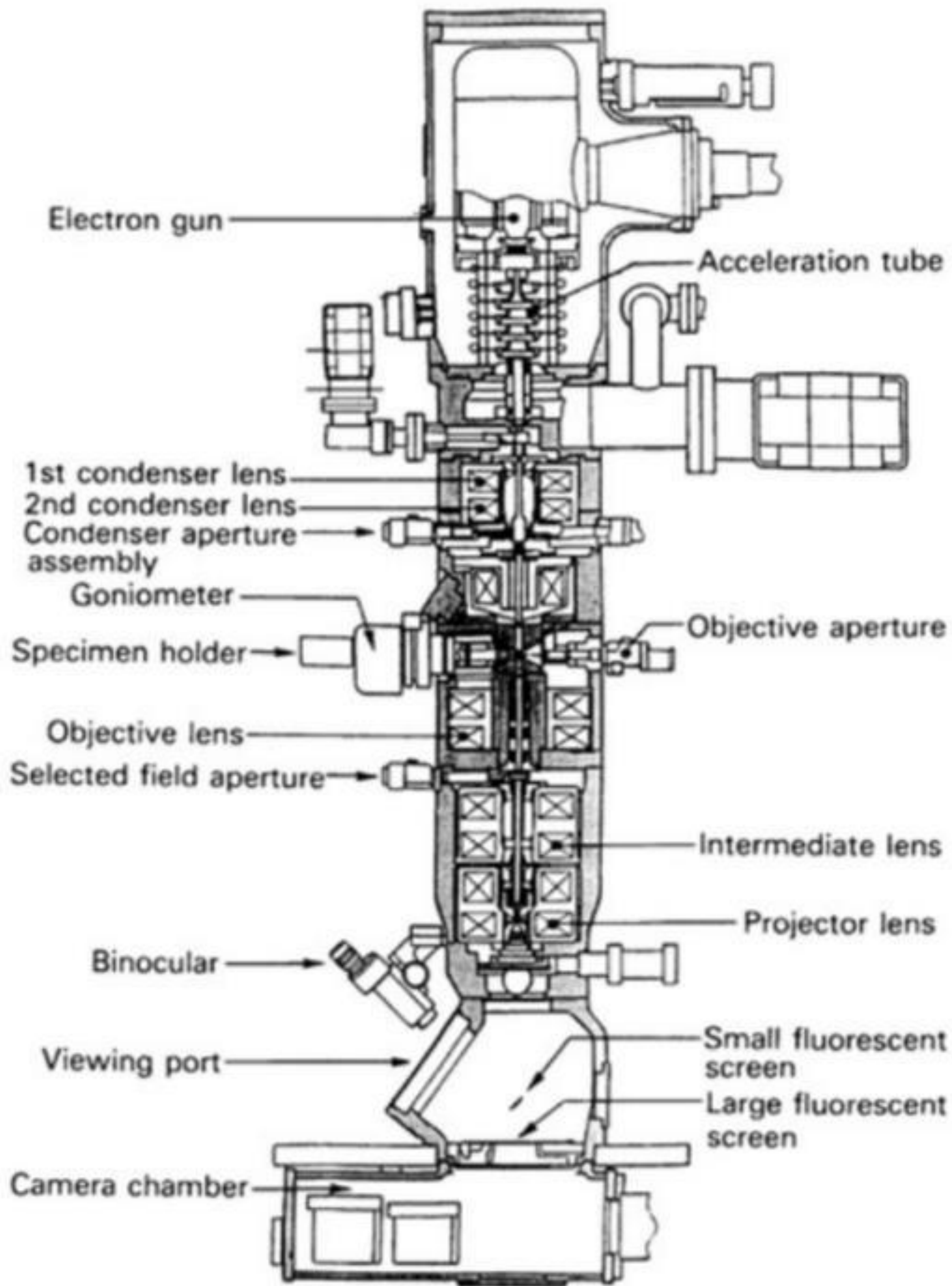

Figure 2.3: Standard TEM with major parts labeled.[23]

There are several different operating modes for TEM imaging and for collecting analytical data. Conventional imaging involves illuminating the sample with an almost parallel beam of electrons. A small objective aperture is used to select specific diffracted electron beams to form an image with diffraction contrast.[24] In contrast, high-resolution TEM (HRTEM) forms an image that is dominated by phase contrast when using a large aperture or no aperture at all. This latter process allows many scattered electron beams to interfere and produce an image with high spatial resolution but often at the cost of generally decreased image contrast.[24] The HRTEM is capable of resolving crystal structures and defects at the atomic scale.[25]

The scanning transmission electron microscope (STEM) uses a focused beam of electrons that is rastered across the sample in similar fashion to the SEM. The resulting signals can be recorded with a wide variety of detectors to produce different types of images and spectral data. For example, a high-angle annular-dark-field (HAADF) detector collects electrons that have undergone incoherent, large-angle elastic scattering (Rutherford scattering), which is strongly dependent on atomic number Z, and results in a so-called "Z-contrast" image.[24] The small focused probe used in the STEM technique can also be coupled with electron energy-loss spectroscopy and energy-dispersive x-ray spectrometry to provide localized chemical analysis related directly to the structural imaging. The spatial resolution for these analytical techniques is limited by the electron probe size, which also depends on aberrations in the probe-forming lenses, as well as any probe broadening due to finite sample thickness.[18] The focused probe of the STEM results in significantly higher beam current densities than used for normal TEM imaging, which are likely to cause increased sample damage. However, use of a scanned beam also

allows for precise control over the region of the specimen that is irradiated. With care and special consideration for the total beam current density, STEM imaging can sometimes be considered as a low-dose form of microscopy.[24]

Work is constantly ongoing to improve the stability and ultimate performance of transmission electron microscopes. The most significant recent improvement has been the development of aberration correctors.[26] Modern TEMs without aberration correction generally achieve a structural resolution of between 3.0 and 1.0 Å when operating between 100 to 1250 kV.[26] This is comparable to the spacing between atomic columns along low-index zone axes in many crystalline materials. However, this resolution is still not fine enough to distinguish between atomic columns along higher-index zone axes, particularly near the cores of dislocation defects or along interfaces. These limitations can be overcome by aberration correction. The ultimate performance of aberration-corrected TEMs is limited by beam divergence, focal spread, and/or instabilities such as stray magnetic fields or mechanical vibrations.[26] With careful beam and crystal alignment and in carefully controlled environments, aberration-corrected TEMs can routinely achieve resolutions on the sub-Ångstrom scale. There have even been reports of resolution limits of below 50 pm.[27]

2.2 Sample Preparation

In order to take advantage of the extreme resolving power of the TEM, care must be taken to prepare samples that are clean, electron-transparent, and free of artificial damage. Layers of foreign material on any sample surface will likely interfere with image interpretation. Common specimen preparation techniques may cause both structural and chemical changes in the sample, especially near the exposed surfaces.[28] Care must be

taken to minimize these preparation effects and to recognize the artifacts that can be introduced during specimen preparation.[28]

Ideally, the region used for high-resolution imaging should be thinner than ~20 nm. The ideal thickness of the sample depends on the technique being used and the particular sample being imaged. For high-resolution TEM (or phase-contrast) imaging, sample thicknesses of less than 10 nm are generally preferred.[28] Thicker samples will result in multiple scattering which is likely to preclude correct image interpretation.[29] In the case of EDS, more scattering events mean increased signal, but also less localized and hence reduced spatial resolution.[30]

Many different techniques are used for preparing TEM specimens. For most semiconducting materials, common preparation techniques include wedge polishing or mechanical polishing and dimpling followed by ion-milling. Mechanical polishing allows for large areas to be prepared for imaging, and dimpling creates a thickness gradient that is sometimes useful.[31] These methods are generally performed by hand, and are not considered very site-specific. Due to the low milling energy of the ion-mill (generally 0.1 to 5 keV), samples prepared in this manner can result in TEM specimens that are relatively clean and with very little preparation damage. However, ion implantation and physical damage to the surface may still occur. These effects can be minimized using an ion beam angle of incidence less than about 5°.[31] This method is generally less expensive than other methods, although the overall time expended to create a high-quality sample may still be quite lengthy. Considerable skill and patience is required to consistently produce useful specimens using this technique.

2.2.1 Wedge Polishing

Wedge polishing avoids the need for sample dimpling. Instead, the sample is mechanically polished nearly all the way to electron transparency by polishing at a small angle to the sample surface, thus creating a wedge shape. An ion mill is often employed to finish polishing the edge of the sample to electron transparency, as well as cleaning up any residual damage remaining after the mechanical polishing process. While this technique often produces samples more quickly and with greater control over specimen thickness than achieved with a dimpled sample, it also applies more stress to the sample, which thereby limits its application to relatively strong materials that do not fracture as they approach electron transparency.[31]

2.2.2 Focused Ion Beam (FIB)

In many instances, it is important to be able to prepare specimens from very precise sample locations. Thinning with the FIB provides the invaluable ability to target an area on the order of several microns, thus allowing site-specific sample preparation.[32] The FIB also has the benefit that finished specimens can be produced in just a couple of hours.[32] Efforts are in progress to develop an automated TEM sample preparation method using FIB milling.[33]

TEM cross-section specimens produced by FIB milling are prepared by first identifying the region of interest. The area is coated with a protective layer of carbon several tens of nanometers thick using an *in situ* carbon deposition system and the electron beam. A protective layer of platinum, typically of 300-600 nm thickness, is then deposited using an *in situ* Pt gas-injection system, also using the electron beam. The carbon film protects the sample surface from possible Ga implantation, and also serves to

provide a useful amorphous region for TEM alignment.[34] Using the electron beam to deposit these initial layers sequentially enables deposition without causing any damage to the sample surface, albeit at the cost of requiring longer deposition time.[34] A final thick protective layer of Pt is then deposited using the ion beam. Using the ion beam for this purpose results in rapid deposition of the Pt layer. In combination, these layers protect the sample surface from damage during the following TEM sample preparation. The specimen region of interest is then separated from the surrounding material and thinned to electron transparency using a standard *in situ* lift-out procedure.[32]

References

[1] S. Mahajan and K. S. Sree Harsha, *Principles of Growth and Processing of Semiconductors*. McGraw-Hill, 1999, pp. 122-123.

[2] R. J. D. Tilley, *Defects in Solids*. John Wiley & Sons, Incorporated, 2008, p. 85.

[3] S. Mahajan *op. cit.* pp. 123-128.

[4] J. L. Weyher, In *The Encyclopedia of Advanced Materials* "Compound Semiconductors: Defects Revealed by Etching." ed. D. Bloor, R. J. Brook, M. C. Flemings, and S. Mahajan. Oxford: Pergamon Press, 1994, p. 460.

[5] M. Vaghayenegar, K. J. Doyle, S. Trivedi, P. Wijewarnasuriya, and D. J. Smith, "Microstructural Characterization of Defects and Chemical Etching for HgCdSe/ZnTe/Si (211) Heterostructures." Journal of Elec Materi, **48**, 571-582 (2018).

[6] H. Liu, Y. Zhang, Y. Chen, and P. S. Wijewarnasuriya, "Confocal Micro-PL Mapping of Defects in CdTe Epilayers Grown on Si (211) Substrates with Different Annealing Cycles." Journal of Elec Materi, **43**, 2854 (2014).

[7] H. K. Henisch, *Electroluminescence*. In: H. K. Henisch, International Series of Monographs on Semiconductors Volume 5. Pergamon Press, 1962, pp. 5-6.

[8] H. K. Henisch *op. cit.* pp. 6-7, 41, 94-104.

[9] H. K. Henisch *op. cit.* pp. 40, 94-96.

[10] R. J. D. Tilley *op. cit.* pp. 8-9.

[11] S. Mahajan *op. cit.* pp. 26-34.

[12] H. K. Henisch *op. cit.* pp. 96-104.

[13] H. K. Henisch *op. cit.* pp. 104-107.

[14] J. L. Crozier, E. E. van Dyk, and F. J. Vorster, "High Resolution Spatial Electroluminescence Imaging of Photovoltaic Modules." Vor. Nelson Mand. Metrop. Univ. (2009).

[15] D. A. Cullen, D. J. Smith, A. Passaseo, V. Tasco, A. Stocco, M. Meneghini, G. Meneghesso, and E. Zanoni, "Electroluminescence and Transmission Electron Microscopy Characterization of Reverse-Biased AlGaN/GaN Devices." IEEE Transactions on Device and Materials Reliability, **13**, 126-135 (2013).

[16] J. I. Goldstein, D. E. Newbury, J. R. Michael, N. W. M. Ritchie, J. H. J. Scott, and D. C. Joy, *Scanning Electron Microscopy and X-Ray Microanalysis*. Springer, 2003, pp. 22-24.

[17] J. I. Goldstein *op. cit.* pp. 40-42.

[18] J. I. Goldstein *op. cit.* p. 2.

[19] J. I. Goldstein *op. cit.* pp. 195-197.

[20] D. B. Williams and C. B. Carter, *Transmission Electron Microscopy: A Textbook for Materials Science, Second Edition.* Springer, New York, 2009, p. 5.

[21] D. B. Williams *op. cit.* p. 86.

[22] D. B. Williams *op. cit.* p. 98.

[23] B. Fultz and J. Howe, *Transmission Electron Microscopy and Diffractometry of Materials*, Springer-Verlag, Berlin Heidelberg, 2013.

[24] D. B. Williams *op. cit.* pp. 372-389.

[25] M. A. O'Keefe, L. F. Allard, and D. A. Blom, "HRTEM imaging of atoms at sub-Ångström resolution." Journal of Electron Microscopy, **54**, 169-180 (2005).

[26] D. J. Smith, "Development of aberration-corrected electron microscopy." Microsc. Microanal. **14**, 2–15 (2008).

[27] R. Erni, M. D. Rossell, C. Kisielowski, and U. Dahmen, "Atomic-Resolution Imaging with a Sub-50-pm Electron Probe." Physical Review Letters **102**, (2009).

[28] D. B. Williams *op. cit.* p. 11.

[29] D. B. Williams *op. cit.* p. 26.

[30] D. B. Williams *op. cit.* pp. 597, 663-665.

[31] D. B. Williams *op. cit.* pp. 177-182.

[32] M. H. F. Overwijk, F. C. Van den Heuvel, and C. W. T. Bulle-Lieuwma, "Novel scheme for the preparation of transmission electron microscopy specimens with a focused ion beam." Journal of Vacuum Science & Technology B: Microelectronics and Nanometer Structures Processing, Measurement, and Phenomena, **11**, 2021-2024 (1993).

[33] J. Y. Dai, S. F. Tee, C. L. Tay, Z. G. Song, S. Ansari, E. Er, and S. Redkar, "Development of a rapid and automated TEM sample preparation method in semiconductor failure analysis and the study of the relevant TEM artifact." Microelectronics Journal, **32**, 221-226 (2001).

[34] D. A. Cullen and D. J. Smith, "Assessment of surface damage and sidewall implantation in AlGaN-based high electron mobility transistor devices caused during focused-ion-beam milling." Journal of Applied Physics, **104**, 094304 (2008).

CHAPTER 3

ETCH PITS IN CdTe EPILAYER

This study was intended to correlate individual structural defects in CdTe epilayers with their corresponding optoelectrical behavior in order to provide better understanding of how these defects affect device operation. The work was carried out in collaboration with Professor Yong Zhang and his group at the University of North Carolina at Charlotte, who were responsible for gathering optical and electrical data from the CdTe epilayer material, chemically treating the surface, and correlating the resulting surface etch pits with optical and electrical measurements. The TEM sample preparation and characterization was performed by the present author.

3.1 Introduction

In order to correlate the atomic structure of individual defects with specific optical properties of a working optoelectronic device, it is essential to characterize both the structure and the optical properties of the same defect. Previous work has shown that cathodoluminescence (CL) and TEM can be used in tandem to correlate optical transitions with extended defects in GaN.[1] However, this study did not report the achievement of atomic-scale resolution and did not demonstrate any effect of an individual defect on the material's optical properties. Another recent study correlated photoluminescence (PL) imaging, chemical etching, and SEM imaging in CdTe epilayers and concluded that etch pits resulting from the etching did not always match with the dark spots visible in PL imaging.[2] Moreover, while PL imaging is preferable to chemical etching for indicating the impact of defects on device operation because the sample is

undamaged during examination, it does not reveal how the carriers are generated, injected, or extracted.

Single-crystal CdTe has a long history of use in solar-cell devices, primarily because it has material properties that are nearly ideal for thin-film photovoltaic applications.[3,4] Not only does it have an optical band gap that is close to the optimum for solar energy conversion, but it is also relatively easy to handle during thin-film deposition and processing.[4] More recent studies have also shown that polycrystalline CdTe solar cells can operate with higher efficiency than single-crystal CdTe devices, suggesting that crystal defects or impurities contribute to the ultimate device efficiency.[5,6]

This current study has employed electroluminescence (EL) mapping and chemical treatment of the surface of a CdTe epilayer in order to isolate individual defects associated with localized disturbances in device performance. Samples suitable for TEM observation were then prepared using the FEI Nova 200 NanoLab which combines a high-resolution SEM with a focused ion beam (FIB) to allow for site-specific TEM sample preparation with sub-micron precision. The work described here focuses on the practical challenges associated with TEM sample preparation of locations which were previously identified by chemical etch pits on the rough surface.

3.2 Experimental Details

In this study, the sample consisted of a 6-μm CdTe film grown on a 50-nm ZnTe buffer layer on a Si substrate. This sample had been chemically etched, producing pits where the film surface had been preferentially etched, and it was presumed that the etched sites were due to crystal defects located near the sample surface.[7,8] While surface

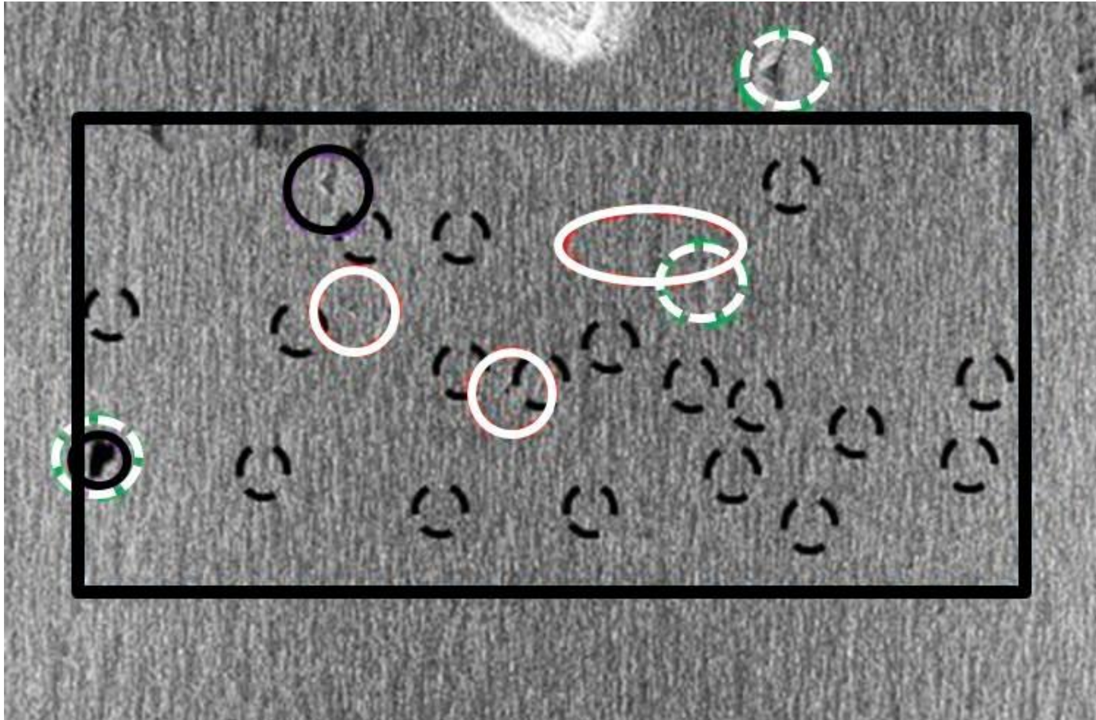

Figure 3.1: SEM image showing chemical etch pits on CdTe epilayer surface. Solid rings indicate loose correlation of etch pits with dark PL spots, with white rings indicating more confidence than black. Broken rings indicate uncorrelated features: white for etch pits and black for dark PL spots. (From Professor Yong Zhang at the University of North Carolina-Charlotte.)

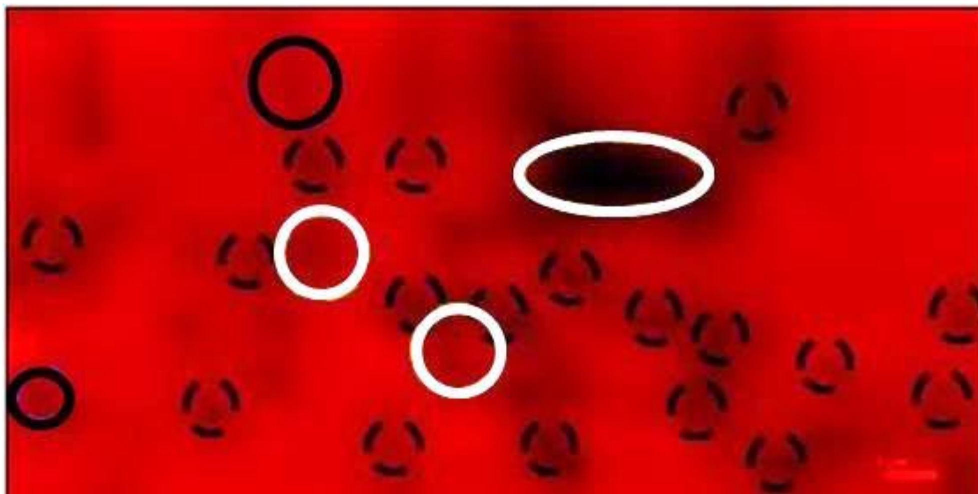

Figure 3.2: PL map corresponding to area indicated by the rectangle in figure 3.1. (From Professor Yong Zhang at the University of North Carolina-Charlotte.)

pits were readily observed in the SEM, electroluminescence was also employed in an attempt to identify other important defects of interest.

Figure 3.1 is an SEM image showing typical examples of surface etch pits, highlighted by solid black or white circles, as well as dashed white circles. Solid rings indicate loose correlation of etch pits with dark PL spots, with white rings indicating more confidence than black. Broken rings indicate uncorrelated features: white for etch pits and black for dark PL spots. The noisy appearance of figure 3.1 is a result of the sample's rough surface, which is caused by the etching process. Etch pits that were deeper and wider than the average roughness of the surrounding surface were relatively easy to identify, while smaller etch pits might have been missed. This is particularly true when the surface is viewed in cross-section as done during TEM sample preparation. Figure 3.2 shows a PL map corresponding to the area marked in figure 3.1. A close comparison of Figs. 3.1 and 3.2 indicates that not every surface pit corresponds to a dark spot in the PL map, or that every dark spot in the PL map corresponds to an etch pit on the surface. This study has focused on analyzing locations on the CdTe device where the surface etch pits visible in the SEM images corresponded directly to dark spots in the PL map.

3.3 Results and Discussion

Identifying defects in this CdTe sample that corresponded to the etch-pit locations ultimately proved to be unsuccessful. Etch pits in the studied material tended to be long and narrow with depths that were shallow compared to their length. As evident in figure 3.3, when an etch pit was chosen with depth much greater than the surrounding surface roughness, then the pit was easily recognized during the TEM sample preparation.

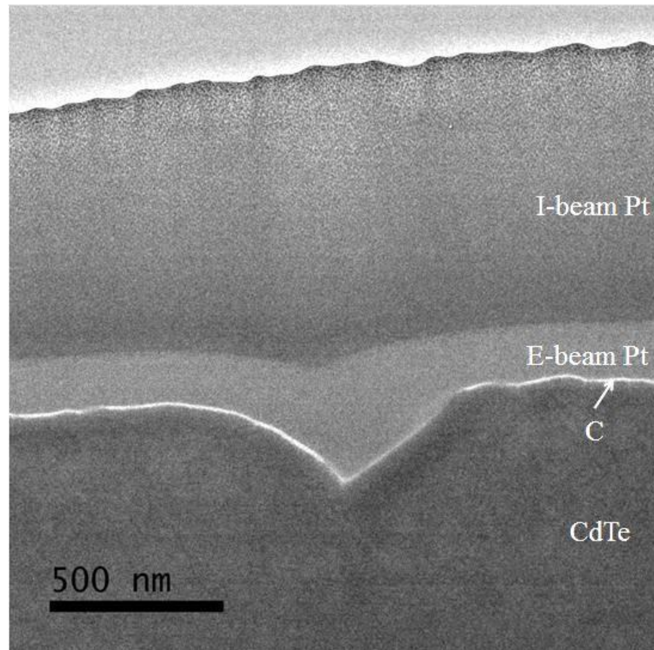

Figure 3.3: TEM image showing a cross section of a large etch pit in a thick CdTe epilayer grown on ZnTe/Si composite substrate.

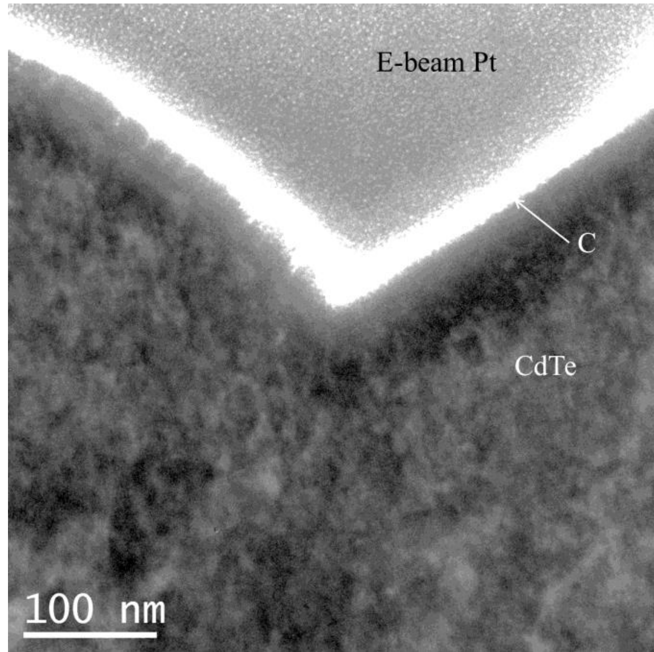

Figure 3.4: TEM image at higher magnification showing the base of the etch pit visible in figure 3.3. Mottled contrast due to surface damage that occurred during FIB milling.

However, thinning the sample to electron transparency while still preserving the region of interest at the deepest point of the pit was challenging due to the shallow incline of the pit's surface. Figure 3.4 is a TEM image at higher magnification showing the base of the etch pit in figure 3.3. While the etch pit is clearly identifiable, there is no evidence of any defect at or near the base of the etch pit. It is possible that no defects were present because the specimen was incorrectly centered on the etch pit. Thus, the deepest point of the etch pit, where the defect is most likely to be located, might have been milled away during sample preparation. On the other hand, if the defect responsible for the formation of the pit extended no further into the sample than the final depth of that pit, then the defect would have been completely destroyed during the etching process. Thus, shallower etch pits are more likely to indicate the locations of defects that have not been entirely removed during etching. Furthermore, careful comparison of figures 3.1 and 3.2 revealed that smaller etch pits tended to correspond to darker areas in the PL map rather than larger etch pits, while many of the darkest spots in the PL map did not seem to correspond to any pit at all.

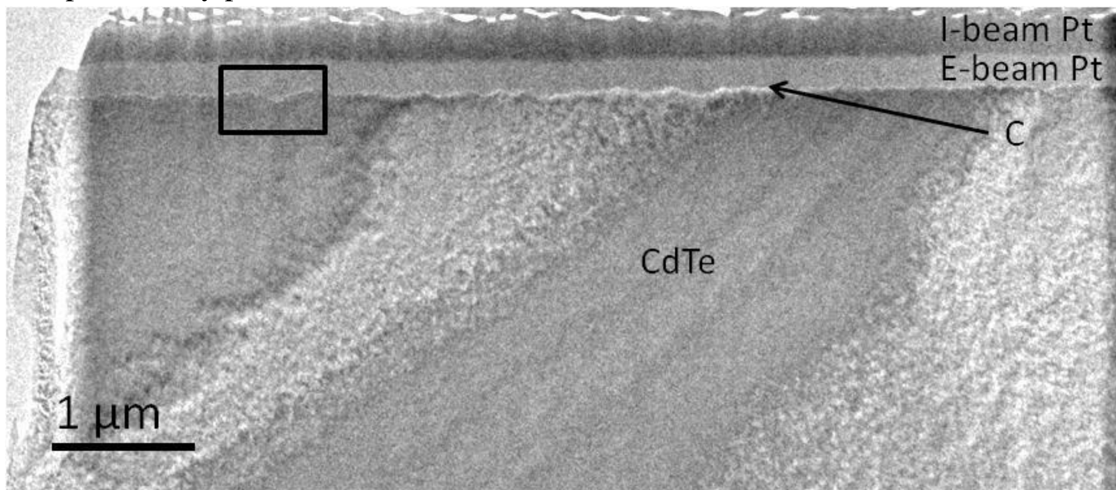

Figure 3.5: TEM cross-section image of a CdTe epilayer sample where a relatively small etch pit was targeted. The possible location of the small etch pit is indicated by a black rectangle.

Selection of a small etch pit as the location for TEM sample preparation often resulted in a specimen where it was difficult to identify the region of interest, both during sample preparation and in the resulting TEM image. Figure 3.5 is a TEM image of a specimen where a small etch pit was selected for sample preparation. The area marked by the black rectangle could be part of the small etch pit since the sample surface is lowest at that location. However, the surface profile in this region is very similar to the rest of the specimen surface, suggesting that this feature could simply be a particularly deep furrow in the rough surface rather than the etch pit. TEM specimens such as this were all-too-common due to the difficulty of accurately identifying the region of interest when thinning the specimen to electron transparency.

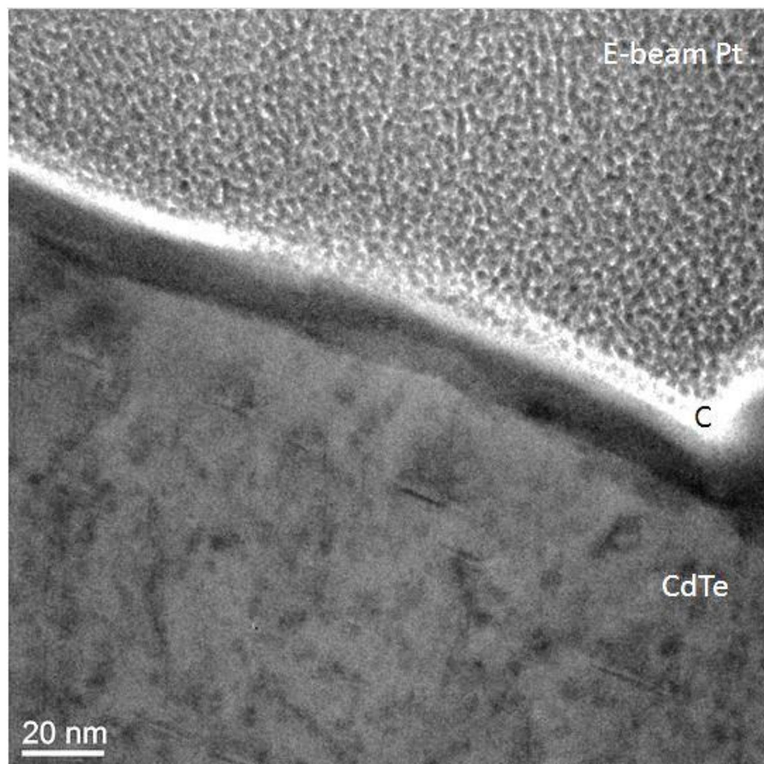

Figure 3.6: TEM image at high magnification showing the base of the pit marked by the red rectangle in figure 3.5. Note the presence of short stacking defects below the surface in the CdTe layer that were possibly caused by TEM sample preparation.

Figure 3.6 shows a higher magnification TEM image of the area marked by the black rectangle in fig. 3.5. While there are many small defects near the sample surface at the base of this pit, they do not appear to be directly associated with the pit. Rather, these defects are more likely to be the result of damage caused during TEM sample preparation.[9] This observation further suggests that this pit is simply a furrow in the sample surface rather than being an etch pit of interest.

3.4 Conclusions

Identifying specific sites of possible crystal defects in CdTe epilayers through the use of EL mapping, and the creation of surface etch pits through chemical treatment, should in principle be possible. However, this study only produced TEM specimens of etch pits, and there were no signs of extended defects at their base. Thus, the primary obstacle impeding progress in this research has proven to be the experimental difficulty of identifying etch pits for study that corresponded to locations of decreased optical and electrical activity, as shown by EL mapping, and were of the right size, i.e., not so shallow as to become indistinguishable from the surrounding surface roughness but not so deep that the defect of interest has already been completely removed by the etching process.

It is finally concluded that while the formation of etch pits could theoretically prove beneficial for precisely locating extended defects associated with decreased optoelectrical activity, the resultant surface roughness surrounding etch pits mitigates against their usefulness. A similar study in which optoelectrically active defects are located through the use of EL mapping, or similar techniques, and their locations precisely measured relative to recognizable surface features, would result in a higher

percentage of extended defects being successfully isolated for TEM characterization and successive correlation with device properties. Alternatively, reasons explaining why EL dark spots and the locations of surface etch pits do not generally correspond to each other could be more effectively investigated by selecting a material system where chemical etching is less destructive to non-defective material relative to defect sites.

References

[1] G. Salviati, M. Albrecht, C. Zanotti-Fregonara, N. Armani, M. Mayer, Y. Shreter, M. Guzzi, Yu. V. Melni, K. Vassilevski, V. A. Dmitriev, and H. P. Strunk, "Cathodoluminescence and transmission electron microscopy study of the influence of crystal defects on optical transitions in GaN." Physica Status Solidi (a), **171**, 325-339 (1999).

[2] H. Liu, Y. Zhang, Y. Chen, and P. S. Wijewarnasuriya, "Confocal Micro-PL Mapping of Defects in CdTe Epilayers Grown on Si (211) Substrates with Different Annealing Cycles." Journal of Elec Materi **43**, 2854 (2014).

[3] P. V. Meyers, "Design of a thin film CdTe solar cell." Solar cells, **23**, 59-67 (1988).

[4] C. S. Ferekides, D. Marinskiy, V. Viswanathan, B. Tetali, V. Palekis, P. Selvaraj, and D. L. Morel, "High efficiency CSS CdTe solar cells." Thin Solid Films, **361**, 520-526 (2000).

[5] L. M. Woods, D. H. Levi, V. Kaydanov, G. Y. Robinson, and R. K. Ahrenkiel, "Electrical characterization of etched grain-boundary properties from as-processed px-CdTe-based solar cells." In AIP Conference Proceedings, **462**, 499-504. American Institute of Physics, (1999).

[6] C. Li, J. Poplawsky, Y. Yan, and S. J. Pennycook, "Understanding individual defects in CdTe thin-film solar cells via STEM: From atomic structure to electrical activity." Materials Science in Semiconductor Processing, **65**, 64-76 (2017).

[7] R. J. D. Tilley, *Defects in Solids*. John Wiley & Sons, Incorporated, 2008, p. 85.

[8] S. Mahajan and K. S. Sree Harsha, *Principles of Growth and Processing of Semiconductors*. McGraw-Hill, 1999, pp. 122-123.

[9] J. Belz, A. Beyer, T. Torunski, W. Stolz, and K. Volz, "Direct investigation of (sub-) surface preparation artifacts in GaAs-based materials by FIB sectioning." Ultramicroscopy, **163**, 19-30 (2016).

CHAPTER 4

STRUCTURAL DEFECTS IN GaAs SOLAR CELLS

This chapter describes an investigation of GaAs solar cells, carried out in collaboration with Professor Yong Zhang and his group at the University of North Carolina at Charlotte, who were responsible for collecting optical and electrical data from actual devices and identifying locations of decreased optoelectrical activity. The TEM sample preparation and structural characterization of the devices presented here were performed by the current author.

4.1 Introduction

The compound semiconductor GaAs has been extensively used for photovoltaic devices since the early 1960s when the first LEDs and semiconductor lasers were developed.[1] Continued research has led to the development of GaAs thin-film solar cells which can have efficiencies as high as 28.8%.[2] Because GaAs has been so well characterized, and the effects of its intrinsic materials properties on GaAs-based devices are already well known, it is an ideal material for this current investigation which has focused on the correlation between defect structure and device performance.

Photovoltaic devices are most often characterized in terms of their light conversion efficiency, and many practical factors will contribute to the ultimate efficiency actually attained. Maximizing device efficiency generally depends on optimizing such characteristics as surface texture, layer thickness, and crystallinity. Moreover, it has been shown that crystal defects play an important role in determining device performance for single-crystal and polycrystalline devices.[1,3,4,5,6]

Crystal defects can be considered in terms of two main categories: point defects (PDs) and extended defects (EDs).[7] Point defects typically only involve one atom, or maybe just a few, and take the form of substitutional or interstitial foreign atoms, vacancies, or anti-site defects. Conversely, EDs can consist of hundreds of atoms or more that are displaced from their regular lattice sites. Examples of these types of EDs include dislocations, precipitates, and grain boundaries. While different kinds of defects will each have uniquely distinct electronic structure, it is generally true that an ED contributes a much higher density of states to the band structure of a semiconductor device than even a moderate number of PDs. Consequently, device applications that involve low carrier densities tend to be impacted more by PDs whereas EDs play a more important role in high-carrier-density applications, because the high carrier density can saturate PDs unlike EDs.[8] Moreover, while PDs often degrade device performance, EDs can degrade a device even to the point of total device failure. However, because of the practical difficulty of carrying out *operando* device characterization at the level of individual defects, important details correlating the interaction between EDs and device performance remain unclear. This study has focused on characterizing individual defects and defect clusters in GaAs solar-cell devices with the overall goal of reaching a better understanding of the impact that these defects have on device performance.

4.2 Experimental Details

This correlative investigation was carried out using a GaAs solar cell that was comprised of many independent sub-cells. The structure of each cell, from bottom to top, was as follows: *p*-type GaAs substrate, 80-nm *p*-type GaAs buffer layer, 50-nm *p*-type GaInP back-surface confinement layer, 3-µm *p*-type GaAs absorber layer, 40-nm *n*-type

GaInP Window	0.05 μm
GaAs Emitter	0.04 μm
GaAs Absorber	3.0 μm
GaInP BSCL	0.05 μm
GaAs Buffer	0.08 μm
GaAs Substrate	

Figure 4.1: Diagram of the GaAs solar-cell device, not drawn to scale.

GaAs emitter layer, and 50-nm *n*-type GaInP window layer. The device structure is shown schematically in fig. 4.1.

The GaAs samples were characterized optically and electronically through the use of photoluminescence (PL), electroluminescence (EL), Raman scattering, and I-V measurements. In previous work by our collaborators, the approximate locations of individual defects in the GaAs layer of GaAs/GaInP heterostructures were typically identified using a low-magnification PL imaging system, and high-resolution PL mapping was then performed to determine defect locations more precisely.[8] However, the GaAs absorber layer in the solar-cell devices investigated in this study produced much weaker PL signals, resulting in no significant defects being detected in these devices using this approach. Thus, EL imaging was used, and was found to provide much higher sensitivity and improved efficiency in locating isolated, optoelectrically active defects. Localized defects typically appear as dark spots in an EL image. Because the defects of interest possess unique spectroscopic features that differentiate them from other irregularities, Raman and PL mapping were carried out at the locations of EL dark spots in order to confirm that these features corresponded to real structural defects in the absorber layer. Microscopic I-V curves were also obtained by separately focusing a 532-

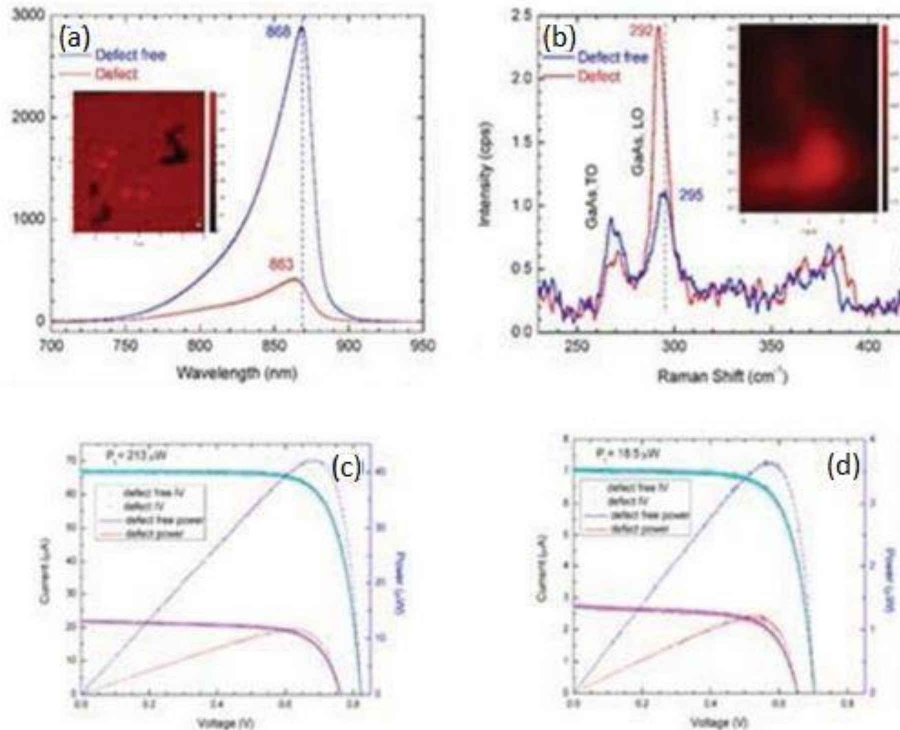

Figure 4.2: Results from (a) PL mapping, (b) Raman scattering, and (c,d) I-V measurements. All spectra and I-V measurements were taken from both a defect location and defect-free location for comparison.[9]

nm laser beam onto the region of the defect site and then away from the defect site, and the results were analyzed to determine the impact of the specific defect on key solar-cell performance parameters. These included short circuit current I_{sc}, open circuit voltage V_{oc}, fill factor FF, shunt resistance R_{sh}, and energy conversion efficiency η.

Examples of results obtained using Raman scattering and I-V measurements are shown in fig. 4.2. The inset in fig. 4.2(a) is a PL map revealing the positions and shapes of potential defects. As expected, the PL intensity from a defect spot is much lower than that from a defect-free spot. Figure 4.2(b) compares the Raman spectra to verify that the defect spot is indeed of possible interest. The I-V curves shown in figs. 4.2(c) and (d) confirm that the region of the defect exhibits drastically degraded light conversion efficiency through reduction in key solar cell parameters.[9]

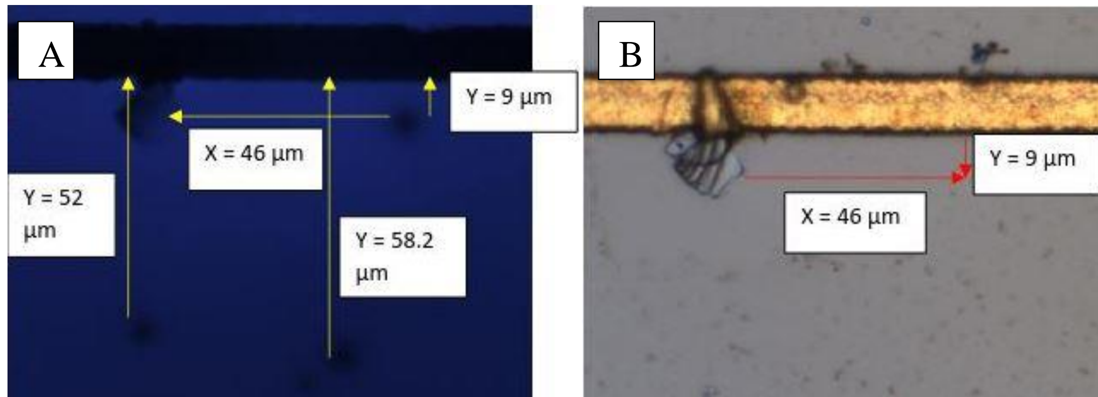

Figure 4.3: Images showing the location of a defect of possible interest. (A) EL map showing three dark spots indicating possible defects. (B) Corresponding optical image showing location of defect relative to identifiable surface features. (From Professor Yong Zhang at the University of North Carolina-Charlotte.)

Figure 4.3a is an EL map and shows how defect locations are precisely located so that they could be found again with the SEM that was used during our FIB TEM sample preparation, despite there often not being any discernible surface feature(s) at the defect locations. This particular EL map was taken simultaneously with an optical image, which allowed the positions of the dark spots to be determined with respect to nearby recognizable surface features. As illustrated in fig 4.3b, these measurements could then be used to identify the same location for TEM sample preparation. This approach is in marked contrast to the conventional method of studying devices where a wafer is typically divided into multiple pieces for parallel optical, structural, and device fabrication and evaluation, and provides no definitive correlation between the structural defect causing the degraded device performance.

An FEI Nova 200 NanoLab (FIB) was used in these experiments since it facilitated site-specific TEM sample preparation with sub-micron precision. Specimens were prepared for observation in [110] projection to enable clear identification of any structural defects present in the device. For better visibility, the specimens were further

milled using a Precision Ion Polishing System (PIPS) operated at 1.8 keV, with the sample cooled to liquid-nitrogen temperature to minimize ion-milling artefacts. A Philips CM200-FEG high-resolution TEM operated at 200 keV was used for initial imaging and atomic-resolution images were taken with a probe-corrected JEOL ARM200F STEM at 200 keV.

4.3 TEM Observations

Several defect sites were identified and suitable cross sections were prepared for TEM characterization. Figure 4.4a shows a TEM image of one such defect location, as identified previously by EL. The dark image contrast indicates a cluster of defects extending downwards from the surface of the solar cell into the GaAs absorber layer, mostly along a {111}-type crystallographic direction. These defects penetrated about 1 μm into the GaAs absorber layer, but did not extend all the way down to the back-surface confinement layer. Figure 4.4b is a bright-field STEM image taken at higher magnification showing the area indicated by the red rectangle in fig. 4.4a. Figures 4.5 and

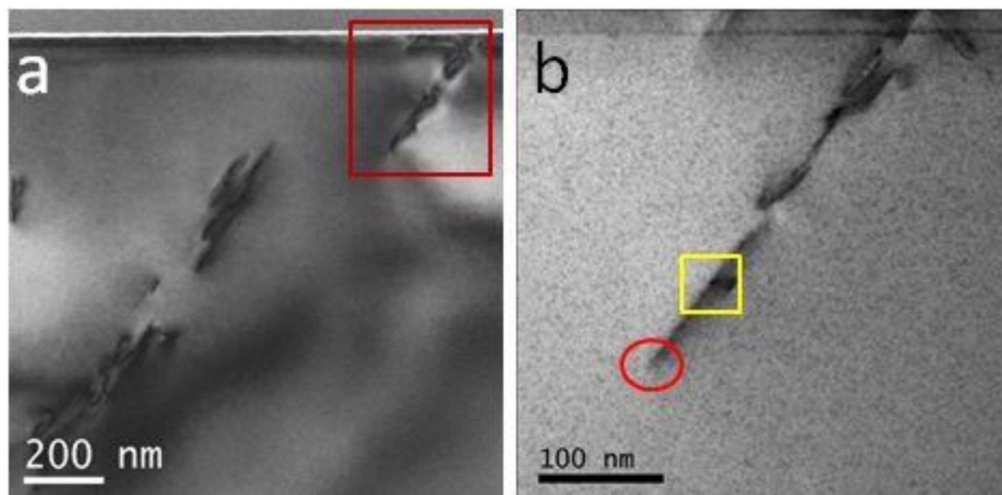

Figure 4.4: (a) TEM image, recorded in [110] projection, of defect cluster in GaAs solar cell device, identified by EL. (b) Higher magnification STEM image of the area highlighted by the square in (a). The red circle and yellow square indicate the locations of figures 4.5 and 4.6, respectively.

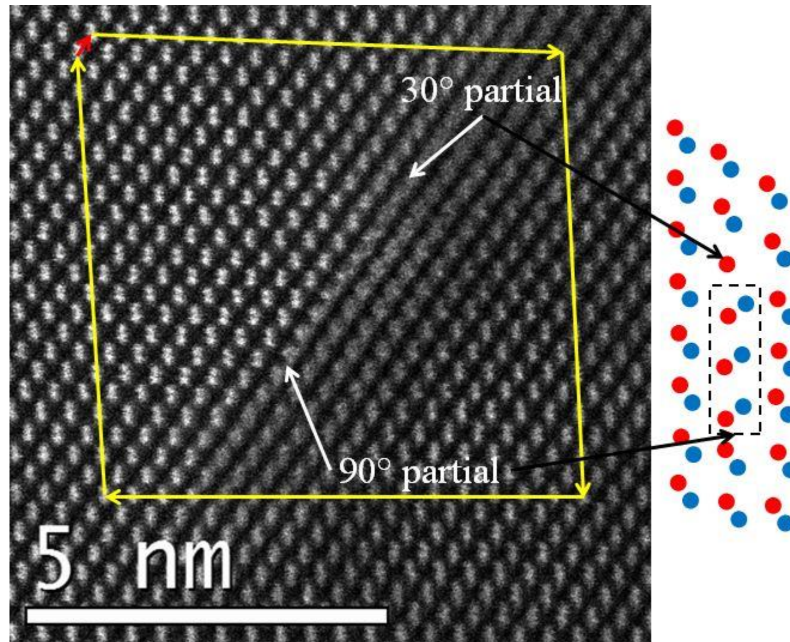

Figure 4.5: HAADF STEM image of 30° and 90° partial dislocations associated with an intrinsic stacking fault in GaAs solar-cell device imaged in [110] projection. (Right) Model of 60° perfect dislocation dissociated into 30° and 90° partial dislocations that terminate an intrinsic stacking fault.

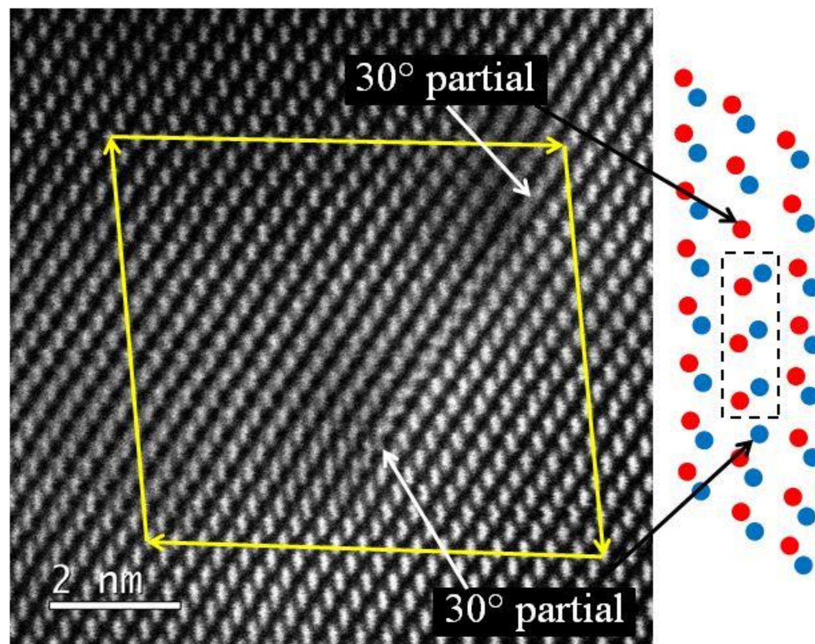

Figure 4.6: HAADF STEM image of two 30° partial dislocations associated with an intrinsic stacking fault in GaAs solar-cell device. (Right) Model of two 30° partial dislocations that terminate an intrinsic stacking fault.

4.6 are high-angle annular-dark-field (HAADF) STEM images taken with atomic resolution at much higher magnification, showing the areas indicated in fig. 4.4b by the red circle, and the yellow square, respectively. Observation of the atomic structure visible in fig. 4.5 reveals an intrinsic stacking fault and the characteristic partial dislocations that terminate each end of this type of defect. The Burgers circuit drawn in yellow identifies the resulting Burgers vector, which is indicated by the red arrow.

The termination of the stacking fault at the top of the image corresponds to an extra plane of atomic columns, indicating that the stacking fault terminates here with a 30° partial dislocation.[10] The lower termination of the stacking fault is not associated with an extra plane of atomic columns, which is consistent with an intrinsic stacking fault terminated by a 90° partial dislocation.[10] A model of a 60° perfect dislocation dissociated into 30° and 90° partial dislocations terminating an intrinsic stacking fault is shown at the right of the image.[10] Although the image resolution is not quite adequate here to determine the chemical identity (Ga or As) of the single atomic column at the core of the 30° partial dislocation, the general structure of the dislocations is in quite reasonable agreement with the structural model.

The Burgers circuit drawn in yellow in fig. 4.6 surrounds two 30° partial dislocations that terminate an intrinsic stacking fault, resulting in a null vector for imaging in this projection. This result indicates that the perfect dislocation, which has split to form an intrinsic stacking fault and two partial dislocations, does not have an edge component. Thus, it seems possible that a perfect screw dislocation has caused the formation of these two partial dislocations.[10] The model to the right of the image schematically illustrates two 30° partial dislocations associated with an intrinsic stacking

fault. The image is less blurred around the core of the dislocation nearer the bottom of the image than at the core of the upper dislocation. However, chemical identification of the single atomic columns (Ga or As?) at the ends of the extra plane of atomic columns associated with these 30° partial dislocations is again limited by the overall image resolution. The general structure of the imaged dislocations still agrees reasonably with the structural model.

Another defect cluster in another GaAs solar-cell device is shown at low magnification in fig. 4.7. This particular defect location is unique in this correlative study since it corresponded to a dark spot in the EL map *and* a smaller white spot in the optical image. As evident in fig. 4.7, the white spot was the result of a pit-like feature near the solar cell surface which is covered over by the GaInP window layer, while the dark spot

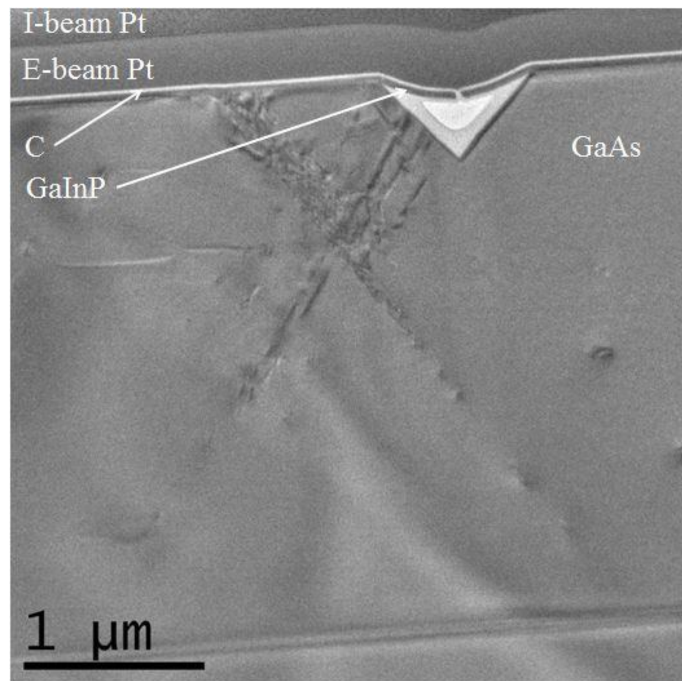

Figure 4.7: TEM image of defect cluster in GaAs solar cell device. Note the presence of a triangular pit beneath the sample surface adjacent to the defect cluster.

in the EL map is presumed to be caused by the defect cluster adjacent to the pit. This defect cluster is very similar in appearance to the cluster shown in fig. 4.4a in that it also extends in {111}-type directions from the surface of the solar cell down into the absorber material, but not all the way through to the back-surface confinement layer. This defect cluster is far more extensive overall, extending at least 2 μm down through the GaAs absorber layer and including many more structural defects, mostly concentrated in the top 1-μm of the absorber layer.

Aberration-corrected STEM (AC-STEM) imaging was used to characterize some of the dislocation cores associated with stacking faults in this cluster. Figure 4.8 is an enlarged view of a Large-Angle Bright-Field (LABF) STEM image which shows where a single 30° partial dislocation terminates an intrinsic stacking fault in the GaAs absorber

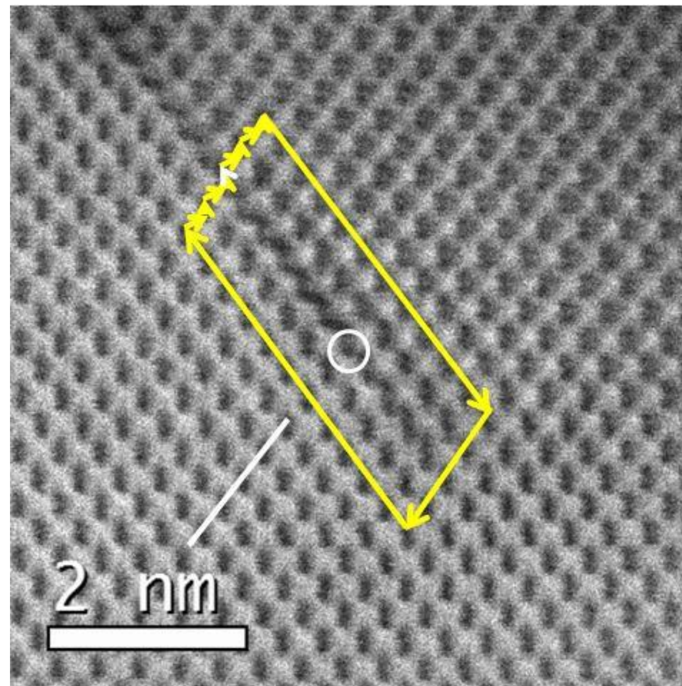

Figure 4.8: Aberration-corrected LABF STEM image of a 30° partial dislocation associated with an intrinsic stacking fault in a GaAs solar-cell device. Individual atomic columns well-resolved.

layer. The type of dislocation was again identified by drawing a Burgers circuit around the defect, as shown with the yellow arrows. The resulting projected Burgers vector is indicated by the white arrow. The partial dislocation is also associated with an extra atomic plane, which is marked in the figure by the white line. The extra atomic plane and the extended stacking fault meet at the dislocation core and are terminated by a single, unpaired atomic column, identified here as corresponding to As, as indicated by the white circle in the figure.

The atomic species of the single atomic column at the dislocation core was determined here by analyzing integrated intensity profiles across nearby atomic columns. Figure 4.9 shows the larger image region from which fig. 4.8 was taken, and the yellow rectangles indicate the regions where the intensity profiles were measured. The intensity profile shown in fig. 4.10 was created by integrating the signals from all 10 individual intensity profiles in order to reduce overall noise in the profile. Each profile begins at the bottom of a rectangle and scans upward. Since this image was recorded in LABF mode, the positions of atomic columns correspond to black spots, or locations of relatively low intensity. However, it is more common to interpret intensity profiles where the peak intensities correspond to atomic columns rather than minimum intensities, so the integrated intensity profile was inverted. Thus, the higher peak intensities in fig. 4.10 actually correspond to the locations of As columns while the lower peak intensities correspond to the locations of Ga columns. Figure 4.10 indicates that the Ga-As dumbbell pairs in fig. 4.8 are oriented with Ga below As. Thus, it follows that the unpaired column situated at the dislocation core corresponds to a column of As atoms.

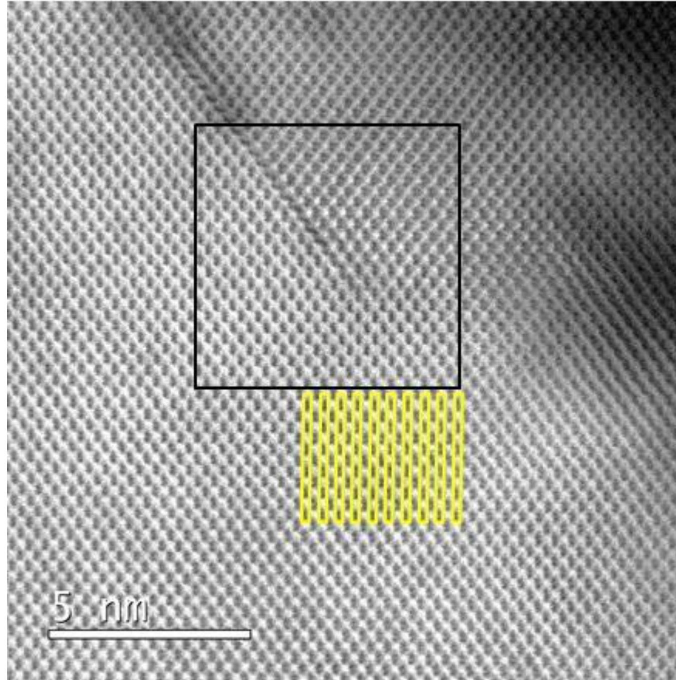

Figure 4.9: LABF STEM image from which fig. 4.8 was taken, as indicated by the box. Yellow rectangles show where intensity profiles were collected by scanning from the bottom to the top of each rectangle.

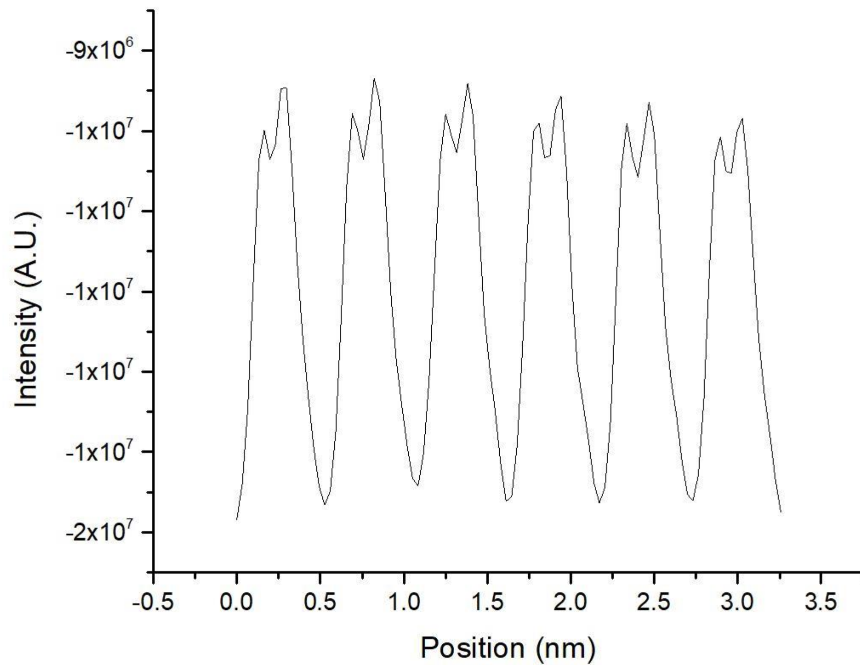

Figure 4.10: Inverted integrated intensity profile of GaAs atomic dumbbells near 30° partial dislocation shown in fig. 4.8. Scans were taken from the bottom of the image going in an upward direction. From the relative profile heights, the lower atomic column in each dumbbell pair of atoms must be comprised of Ga atoms.

Further AC-STEM imaging was carried out where lines of strain contrast intersect in this cluster. Figure 4.11(a) is a LABF STEM image that reveals the presence of a Lomer dislocation at such an intersection. The Burgers circuit drawn to identify the defect is shown in the figure with yellow arrows and the resulting Burgers vector in this projection is indicated by a light blue arrow. Lomer dislocations are commonly associated with two extra atomic planes, indicated in the figure with red lines, which meet at the dislocation core. Figure 4.11(b) is an enlarged view of the dislocation core with the approximate locations of individual atomic columns marked by yellow dots. The white lines in the image show the 5- and 7-member rings commonly associated with Lomer dislocations.[10]

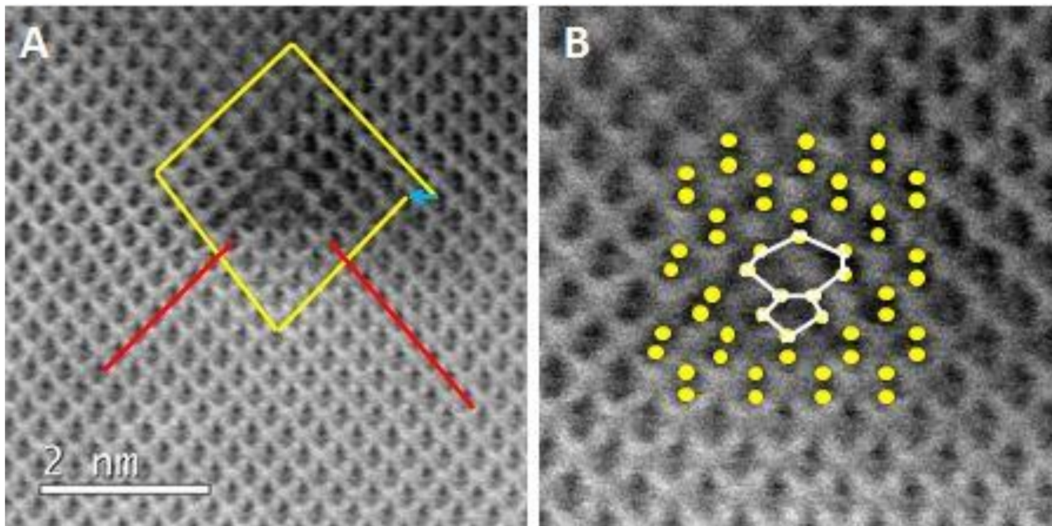

Figure 4.11: (a) LABF STEM image of a Lomer dislocation in the GaAs absorber layer of a solar-cell device. Burgers Circuit shown in yellow and projected Burgers vector shown in light blue. Extra atomic planes terminating at the dislocation core marked by red lines. (b) Enlarged view of the dislocation core region that shows the approximate locations of atomic columns with yellow dots. Ga and As are not distinguished. The 5- and 7-member rings associated with a Lomer dislocation are shown with white lines.[10]

A third defect cluster observed in a third solar-cell device, shown in fig. 4.12, had an overall structure that was markedly different from the previous pair. The GaInP window layer is clearly free of defects in this region. Furthermore, the defect cluster does not extend far into the absorber layer. In fact, this defect cluster is confined mostly to the GaAs emitter layer and extends only a short distance downwards. It is clear that the overall density of defects in the GaAs emitter layer along the GaAs/GaInP interface is higher than in the previous two regions studied and that the defect cluster extends much further laterally along the interface.

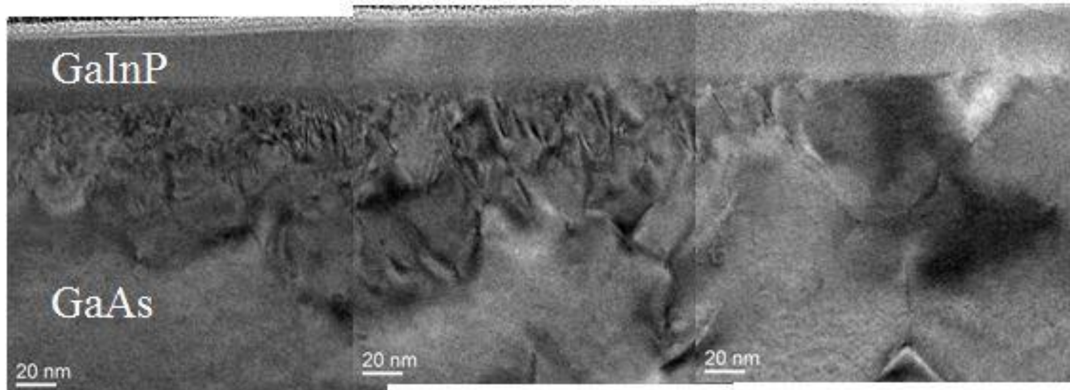

Figure 4.12: TEM images of defect cluster in GaAs solar cell. This cluster extends much further laterally than other clusters along the GaAs/GaInP interface, and yet it also leaves the GaInP layer free of defects.

Individual defects in this cluster were again analyzed using AC-STEM. The HAADF STEM image in fig. 4.13 shows an individual 60° perfect dislocation from this same cluster. The defect was identified by drawing a Burgers circuit, as shown with yellow arrows, and the resulting projected Burgers vector is indicated with a white arrow. A white line marks the extra atomic plane associated with the 60° perfect dislocation.

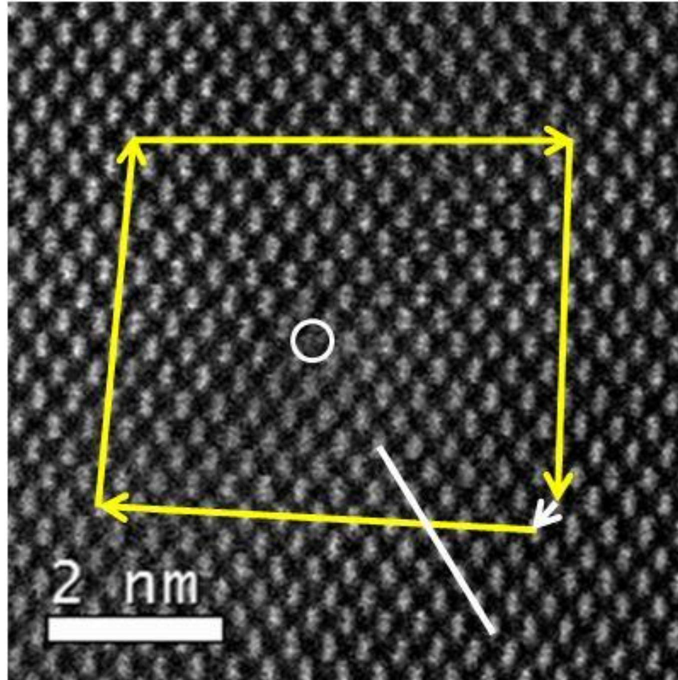

Figure 4.13: HAADF STEM image of a 60° perfect dislocation associated with a single extra atomic plane, indicated by the white line. The Burgers circuit is shown with yellow arrows and the resulting projected Burgers vector is shown with the white arrow.

4.4 Discussion and Conclusions

Defective regions in GaAs solar-cell devices were identified using PL, EL, and Raman, and these were then carefully extracted for TEM analysis. It was found that device degradation was most often associated with a cluster of EDs, rather than by a single ED, as had been previously assumed. Each defect cluster was found to be unique, while still sharing common characteristics. Careful comparison of the different defect clusters showed that every cluster was dominated by a collection of extended {111}-type stacking faults mostly located near the top of the device in the GaAs emitter and absorber layers. However, one defect cluster, with relatively short stacking faults, remained mostly confined to the GaAs emitter layer, leaving the GaInP window layer free of defects and only extending down into the GaAs absorber layer over a short distance (~0.25 μm). The

other two defect clusters analyzed in this study extended from the top of the device, starting in the GaInP window layer, through the GaAs emitter layer, and deep into the GaAs absorber layer; about 1-μm deep in one case and around 2.5-μm deep in the other.

Atomic-scale arrangements of defect clusters were analyzed with AC-STEM. Individual defects in each cluster were found to be comprised primarily of 30° and 90° partial dislocations associated with an intrinsic stacking fault. In a few cases, sufficient resolution was achieved to identify the chemical species of individual atomic columns at the core of 30° partial dislocations. No unpaired atomic columns were found at the cores of 90° partial dislocations.

Although partial dislocations dominated each defect cluster, 60° perfect dislocations and Lomer dislocations were also identified. For example, Lomer dislocations were identified in a large defect cluster adjacent to a surface pit near the location where two lines of strain contrast intersected. Other defect clusters exhibited far fewer of these intersections and no Lomer dislocations were identified in those clusters. A comparatively shallow cluster, largely constrained to the GaAs emitter layer, contained 60° perfect dislocations associated with localized strain contrast, but did not seem associated with any stacking faults. No 60° perfect dislocations were seen in two other clusters, which were dominated by long stacking faults.

References

[1] S. J. Sweeney and J. Mukherjee, (2017) Optoelectronic Devices and Materials. In: Kasap S., Capper P. (eds) Springer Handbook of Electronic and Photonic Materials. Springer Handbooks. Springer, Cham.

[2] M. A. Green, K. Emery, Y. Hishikawa, W. Warta, and E. D. Dunlop, "Solar cell efficiency tables (version 46)." Prog. Photovolt.: Res. Appl., **23**, 805-812 (2015).

[3] C. Li, J. Poplawsky, Y. Yan, and S.J. Pennycook, "Understanding individual defects in CdTe thin-film solar cells via STEM: From atomic structure to electrical activity." Materials Science in Semiconductor Processing **65**, 64-76 (2017).

[4] B. Van Zeghbroeck, Principles of Semiconductor Devices, ECEE Colorado, 2011.

[5] R. J. D. Tilley, *Defects in Solids*. John Wiley & Sons, Incorporated, 2008, p. 85.

[6] G. Salviati, M. Albrecht, C. Zanotti-Fregonara, N. Armani, M. Mayer, Y. Shreter, M. Guzzi, Yu. V. Melni, K. Vassilevski, V. A. Dmitriev, and H. P. Strunk, "Cathodoluminescence and transmission electron microscopy study of the influence of crystal defects on optical transitions in GaN." Physica Status Solidi (a), **171**, 325-339 (1999)

[7] C. Kittel, *Introduction to Solid State Physics.* John Wiley & Sons, Incorporated, 2005.

[8] T. H. Gfroerer, Y. Zhang and M. W. Wanlass, "An extended defect as a sensor for free carrier diffusion in a semiconductor." Applied Physics Letters **102**, 012114 (2013).

[9] Q. Chen, B. S. McKeon, J. Becker, S. Zhang, C.-K. Hu, T. H. Gfroerer, M. W. Wanlass, Y.-H. Zhang, D. J. Smith, and Y. Zhang, "Correlative characterization of dislocation defects and defect clusters in GaAs and CdTe solar cells by spatially resolved optical techniques and high-resolution TEM." *2018 IEEE 7th World Conference on Photovoltaic Energy Conversion (WCPEC),* Waikoloa Village, HI, 2018, pp. 3234-3236.

[10] Y. A. R. Dasilva, R. Kozak, R. Erni, and M. D. Rossell, "Structural defects in cubic semiconductors characterized by aberration-corrected scanning transmission electron microscopy." Ultramicroscopy **176**, 11-22 (2017).

CHAPTER 5

ATOMIC STRUCTURE OF INTERFACIAL MISFIT DISLOCATIONS IN II-VI/III-V HETEROSTRUCTURES

This chapter describes investigations into the atomic-scale structure of misfit dislocations (MDs) in heterovalent ZnTe/GaAs, ZnTe/InP and ZnTe/InAs II-VI/III-V (001) interfaces. Motivations for the work and a brief summary of similar related research are presented. The impact of TEM sample preparation on these heterovalent structures is compared for two preparation techniques: FIB milling and wedge-polishing. Image intensity profiles taken from regions just beside the MDs indicate interfacial diffusion in all three heterostructures, which means that individual atomic columns at MD cores are unlikely to be composed of a single elemental species. The defect cores for ZnTe/InAs ($\Delta a/a \sim 0.74\%$) are primarily 60° dislocations and belong to the glide set, and the individual, unpaired atomic columns at the dislocation cores contain mostly indium. More Lomer dislocations are visible at the ZnTe/GaAs and ZnTe/InP interfaces which have larger lattice-parameter mismatch. Lomer dislocation cores at the ZnTe/InP interface ($\Delta a/a \sim 3.85\%$) consist of a 10-atom ring and two 5-atom rings, whereas the ZnTe/GaAs interface ($\Delta a/a \sim 7.4\%$) mostly displays conventional shuffle-set Lomer dislocations with 5/7-atom ring structures, although asymmetrical MD core structures are also observed. In both systems, intensity line profiles taken adjacent to the MD locations show that the dislocation cores are displaced slightly upwards from the nominal interfacial plane into the ZnTe layer.

The samples described here were provided by Dr. Xinyu Liu and Professor Jacek Furdyna of Notre Dame University.

5.1 Introduction

Semiconductor superlattices and heterostructures based on compound semiconductors have provided major breakthroughs for the electronics and optoelectronics industries, including the development of devices such as light-emitting diodes, quantum-well infrared photodetectors, and quantum cascade lasers.[1] Research into these structures has been ongoing for many years, although the vast majority of published studies have focused either on isovalent heterostructures where both materials had the same valence, or systems where a compound semiconductor was grown on an elemental semiconductor, such as GaAs on Si.[2-16]

Heterovalent structures achieved by integrating II-VI and III-V compound semiconductors, provide many possibilities for further developments in optoelectronic technology.[17,18] For example, the combination of II-VI/III-V materials could enable photovoltaic devices that access a larger range of the solar energy spectrum.[19,20] These myriad possibilities are illustrated in fig. 5.1, which indicates the band-gap energies and lattice constants of many common elemental and compound semiconductors.[19] For example, ZnTe has a band-gap energy of 2.27 eV at room temperature and effectively covers a shorter-wavelength range of the solar spectrum, while GaAs covers a range with longer wavelength due to its band-gap energy at 1.43 eV.[17,21] The interfaces between heterovalent materials may also provide further opportunities arising from the introduction of interfacial electrostatic dipoles. It has been shown that the simplest interface geometry for a polar (001) heterovalent interface requires a transition across at least two atomic planes.[22] This transition region is necessary assuming only small distortions to the lattice and that no substantial charge accumulation occurs at the

interface.[22] However, a more recent theoretical paper proposes the existence of a two-dimensional electron gas at the CdTe(111)/InSb(111) polar interface.[23] These various possibilities do not consider what effects interfacial dislocations might have on the local abruptness of the heterovalent interface nor their impact on charge accumulation.

All heterostructures introduce strain into an epitaxial structure when there is lattice mismatch between the constituent layers. Lattice mismatch, f, is given by the simple expression

$$f = (a_s - a_t)/a_t \quad (5.1)$$

where a_s is the lattice parameter of the substrate material and a_t is the lattice parameter of the epilayer. Misfit dislocations will be generated at heteroepitaxial interfaces when layer thicknesses exceed specific critical values in order to relieve strain produced by the lattice mismatch. As illustrated in fig. 5.1, epitaxial layers consisting of heterovalent materials would provide better opportunity for closely lattice-matched systems, thus reducing misfit dislocation density, albeit at a possible cost caused by introducing the valence mismatch.[19]

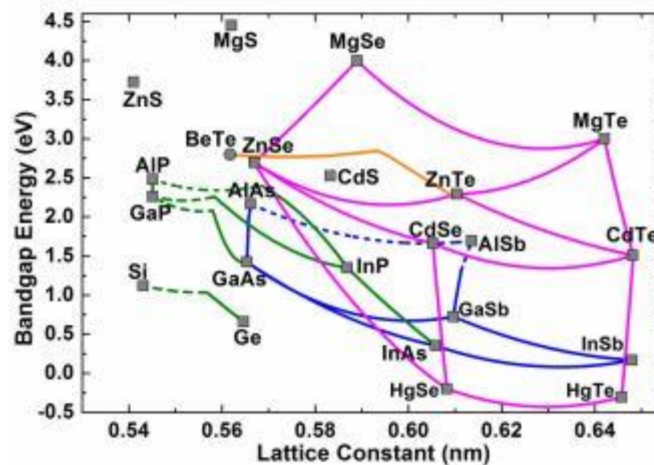

Figure 5.1: Schematic showing band-gap energy vs. lattice parameter of common semiconductor materials.[19]

At interfaces between III-V/III-V semiconductor materials, such as GaSb/GaAs, as well as between elemental semiconductors such as Ge/Si, the misfit strain is normally relieved through the formation of dislocations lying in {111} planes, with Burgers vectors along either <112> directions (60° perfect dislocation) or <110> directions (Lomer dislocation).[7,9,10,12,14-16] The former have frequently been shown to dissociate with a stacking fault and a pair of partial dislocations.[7,9,12,16,24] Hornstra proposed two atomic structures, shuffle type and glide type, for these dislocations, which were later confirmed by experimental observations.[2,10,14,15]

Previous studies of misfit dislocations (MDs) in II-VI/III-V heterovalent systems have shown that interfacial misfit strain is again relieved primarily through the formation of 60° perfect dislocations and 90° Lomer dislocations,[17,20,24-30] with the relative amounts of 60° and 90° dislocations depending on the amount of lattice mismatch.[17] The defect cores in these II-VI/III-V studies were often poorly defined in aberration-corrected electron micrographs, even though individual atomic columns in surrounding material were clearly and unambiguously identifiable from the image intensity.[20,25,26] This chapter reports an experimental study of the atomically-resolved structure of MD cores at lattice-mismatched heterovalent interfaces. Integrated intensity profiles across the interfaces taken away from misfit dislocations show that the interface profiles are not atomically sharp; it is also suggested that increased disorder along dislocation lines is due to increased diffusion very close to the defect core.

5.2 Experimental Details

Samples suitable for examination by transmission electron microscopy (TEM) were prepared from ZnTe/GaAs, ZnTe/InP, and ZnTe/InAs heterostructures, which

consisted of thick (nominally 2.4 μm) ZnTe layers grown on GaAs (001), InP (001) or InAs (001) substrates using molecular beam epitaxy (MBE).[17] The system used for MBE growth consisted of two separate III-V and II-VI chambers connected via an ultrahigh-vacuum transfer module. The substrates were first deoxidized in the III-V chamber, and a corresponding buffer layer was then grown (except in the case of InP), before being cooled and transferred under ultrahigh vacuum to the II-VI chamber. The substrate surface was then irradiated with Zn for ~300 seconds before the thick ZnTe layer was deposited. The substrate temperature was held at 330 °C during the ZnTe growth. The flux ratio of Zn to Te, which was close to 1, was adjusted slightly to optimize film growth, which was also monitored using reflection-high-energy electron diffraction.

Cross-sectional TEM specimens were prepared using one of two methods: *in situ* lift-out using an FEI Nova 200 NanoLab (FIB); or mechanical wedge polishing. Specimens prepared via FIB milling underwent final cleaning of the sample surfaces at an ion-beam energy of 5 keV. Wedge-polished samples were lightly cleaned by ion-beam polishing using a Gatan Precision Ion Polishing System (PIPS) operated at 2 kV with the sample held at liquid nitrogen temperature to minimize ion-milling artefacts. Samples were prepared for observation along two orthogonal {110}-type zone axes. Electron micrographs were recorded using a Philips CM200-FEG high-resolution TEM, operated at 200 kV. Atomic-resolution structure images were recorded using a probe-corrected JEOL ARM200F scanning TEM, also operated at 200 kV. The beam convergence angle was set at 20 mrad, and the collection angles were 0-22 mrad for large-angle bright-field (LABF) imaging and 90-150 mrad for high-angle annular-dark-field (HAADF) imaging.

5.3 Sample Preparation Artefacts

The impact of different TEM sample preparation techniques on these heterovalent II-VI/III-V structures was investigated by comparing cross-sectional electron micrographs of ZnTe/InP and ZnTe/GaAs heterostructures that had been prepared for TEM observation with either FIB milling or wedge polishing. Figure 5.2 compares representative TEM micrographs of: (a) ZnTe/GaAs, and (b) ZnTe/InP samples prepared using FIB milling. The presence of MDs at interfaces in both samples is revealed by periodic modulation of contrast along each interface, although this is much clearer in fig. 5.2(a), appearing almost like a line with alternating light and dark contrast. Figure 5.2 shows that FIB milling tends to result in heavily damaged ZnTe with many short stacking faults, and also leaves the substrate with splotchy, mottled contrast, likely due to surface coverage and some implantation. While the ZnTe layer is heavily damaged for both heterostructures, it seems to be better preserved in the ZnTe/GaAs sample even though the GaAs substrate is apparently more damaged than the InP substrate.

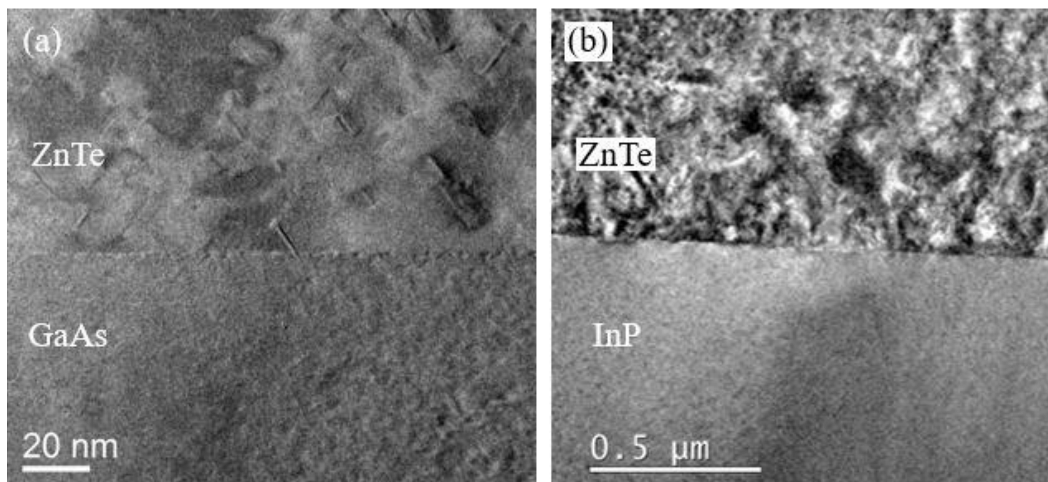

Figure 5.2: TEM images of: (a) ZnTe/GaAs (001) interface and (b) ZnTe/InP (001) interface showing high density of defects in ZnTe epilayer, most likely caused by sample preparation during FIB milling. Alternating light and dark contrast at both interfaces due to the presence of MDs is also visible.

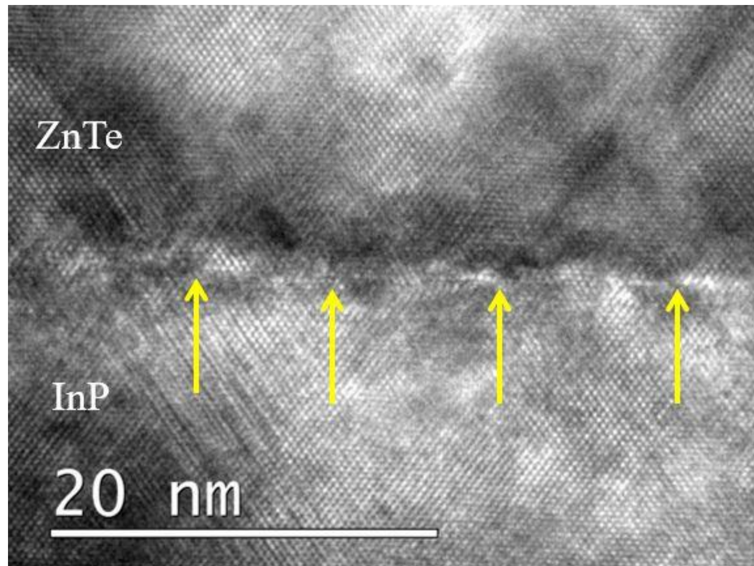

Figure 5.3: Higher magnification TEM image of interface shown in Fig. 5.2(b). Alternating contrast along the interface indicates the presence of MDs. Yellow arrows indicate the approximate location of MDs.

The interface in fig. 5.2(b) is shown at higher magnification in fig. 5.3 where the alternating light and dark contrast due to MDs is more visible and emphasized with yellow arrows. Figure 5.3 also reveals extended stacking faults, possibly due to sample preparation damage, in both the ZnTe layer and the InP substrate.

Figure 5.4 is a typical cross-section image of a ZnTe/GaAs interface prepared for TEM observation by wedge polishing. This image shows that wedge polishing can also results in sample-preparation artefacts, particularly in the form of short {111}-type stacking faults. While the GaAs substrate is not as mottled and splotchy compared to the GaAs substrate seen in fig. 5.2(a), the wedge-polishing method tends to result in more bending and strain, visible in fig. 5.4 as large areas of dark and light contrast as opposed to the relatively uniform contrast seen in fig. 5.2.

A careful comparison of figs. 5.2-4 shows that both FIB milling and wedge polishing can result in damage artefacts, but also indicates that those artefacts are subtly

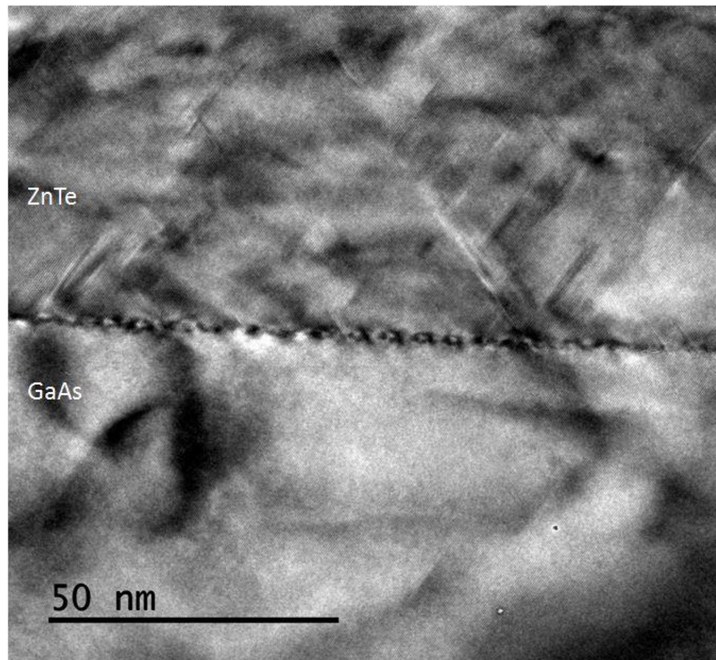

Figure 5.4: TEM image of ZnTe/GaAs interface prepared using wedge polishing. Stacking fault defects in both materials are likely created during wedge polishing or possibly ion-beam cleaning.

different. FIB milling often results in the creation of many short stacking faults, particularly in the ZnTe layer, and also leaves the substrate with splotchy, mottled contrast. On the other hand, wedge polishing also causes stacking faults in ZnTe, but these tend to be a little longer. Furthermore, the substrate appears less mottled, but unfortunately still suffers from contrast variations, likely as a result of bending and thickness variations.

5.4 Interfacial 60° Dislocations

Figure 5.5 shows an example of a 60° perfect dislocation at the ZnTe/InP interface. The Burgers circuit shown in yellow around this dislocation indicates a projected Burgers vector of a/6[1-1-2], as shown by the red line. The single un-paired atomic column at the core of the dislocation, marked by the white circle, is consistent

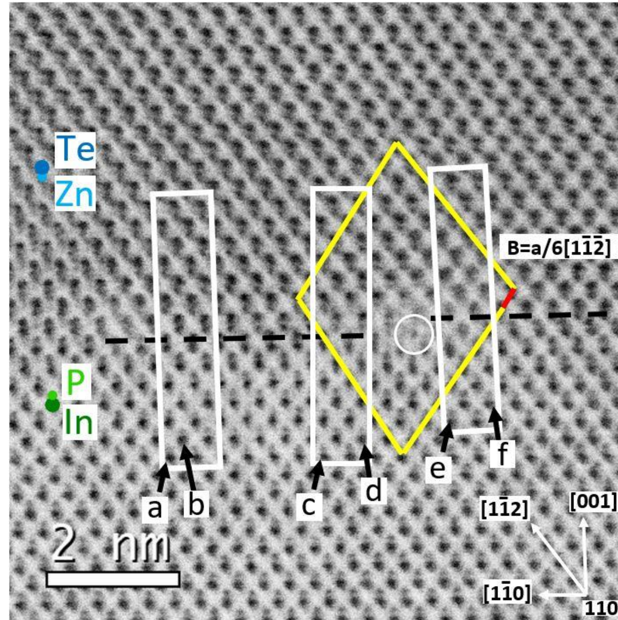

Figure 5.5: LABF STEM image of 60° dislocation at ZnTe/InP (001) interface. Approximate location of nominal interfacial plane indicated with black, dashed lines. White rectangles indicate locations where the intensity profiles shown in figure 5.6 were measured. The individual, unpaired atomic column at the dislocation core is marked with the white circle. Burgers circuit shown with yellow lines and the projected Burgers vector shown with the red line.

with a 60° glide-set dislocation and was determined to consist primarily of In atoms.[12] However, the detailed atomic structure in the vicinity of the dislocation core is unclear.

Figure 5.6 shows integrated intensity profiles from fig. 5.5 taken: (a) away from the dislocation core, and (b and c) near the dislocation core on either side, as indicated by the boxes in fig. 5.5. In order to reduce noise, several line profiles were summed together, skipping a plane of atomic columns between scans so that atomic-column pairs coincided. The skipped atomic planes were measured in the same way to create another series. Locations for the line profiles are labelled alphabetically from the left of fig. 5.5 to the right. Intensity profiles were measured from large-angle bright-field STEM images so that dark spots corresponded to the positions of atomic columns. In order to make the interpretation of the intensity profiles more intuitive, the measured intensities were

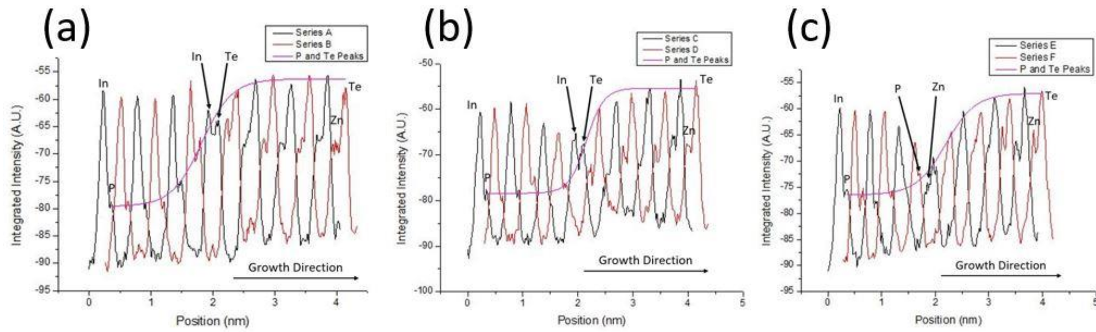

Figure 5.6: Inverted integrated intensity profiles collected from figure 5.5: a) far left, b) just left of dislocation core, and c) just right of dislocation core.

inverted so that peaks in the profile corresponded with atomic column positions. Adjacent series are plotted together with an appropriate sideways shift along the position axis. All intensity profiles are measured in the same direction scanning from the substrate into the ZnTe layer.

Close inspection of the intensity profiles in fig. 5.6 reveals that the interfacial atomic structure changes across the dislocation core. There is a compositional transition layer at the interface to the left of the dislocation, as indicated in figs. 5.6(a) and 5.6(b) with arrows, that is comprised primarily of In and Te columns. There is a step at the location of the dislocation core, so that the interface no longer exhibits III-VI bonding to the right of the dislocation, but instead is made up of Zn-P (II-V) bonds, as indicated by the arrows in fig. 5.6(c).

The intensity peaks, which correspond to positions of the atomic columns, have been fitted with a sigmoidal function, and the width of the curve from 10% to 90% is taken as a measure of the interface width. Approximate interface widths based on this criterion range from 0.72 nm to 1.08 nm. Clearly, the interface is not atomically abrupt, but it rather suffers from chemical intermixing. Moreover, it seems that the nature of the

interdiffusion is altered by closeness to the dislocation core. As seen in fig. 5.6(a), the P to Te transition measured far from the dislocation is shifted slightly down into the InP substrate relative to the nominal interface position whereas the same transition measured on either side of the dislocation core is shifted up into the ZnTe layer, as shown in figs. 5.6(b) and 5.6(c). Thus, it appears that misfit dislocations in II-VI/III-V systems not only facilitate the transition between lattice parameters, but also participate in the relaxation of valence mismatch through local variations in chemical intermixing across the interface.

Similar atomically-resolved defect structures were identified for the ZnTe/GaAs and ZnTe/InAs systems, as shown in figs. 5.7 and 5.8, respectively. The positions of the 60° dislocation cores in both structures corresponded to steps in the interfacial plane. The interfacial step at the ZnTe/GaAs interface corresponded to a transition from II-V bonding to III-VI bonding, as shown in fig. 5.7, which was similar to the transition visible at the ZnTe/InP interface. In contrast, the dislocation core at the ZnTe/InAs

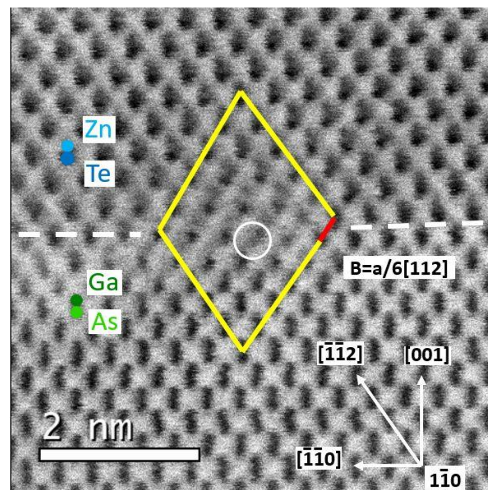

Figure 5.7: LABF STEM image of 60° dislocation at ZnTe/GaAs (001) interface. Approximate location of nominal interfacial plane indicated with white dashed lines, as measured with integrated intensity profiles (not shown). Individual, unpaired atomic column at the dislocation core is marked with the white circle. Burgers circuit shown with yellow lines and resulting projected Burgers vector with the red line.

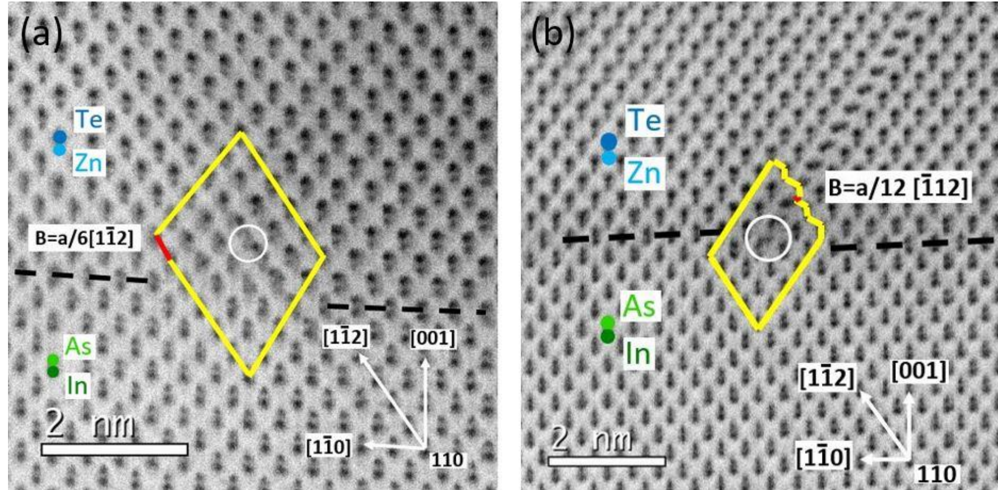

Figure 5.8: LABF STEM images of: (a) 60°, and (b) 30° dislocations at ZnTe/InAs (001) interface. Approximate locations of nominal interfacial planes indicated with black dashed lines, as measured with integrated intensity profiles (not shown). Individual, unpaired atomic columns at the dislocation cores are marked with white circles. Burgers circuits shown with yellow lines and resulting projected Burgers vectors with the red lines.

interfaces, shown in fig. 5.8, corresponded to a double step with the interfacial plane on either side of the dislocations characterized by paired atomic columns of mixed chemical composition. Moreover, fig. 5.8(a) reveals that the 60° dislocation core is located just above the interface in the ZnTe layer, rather than at the interface as seen for ZnTe/InP and ZnTe/GaAs structures. This observation is consistent with a previous report that described 60° dislocations at a CdTe/GaAs interface.[27] However, the defect core in fig. 5.8(b) is again located at the interfacial plane. Figure 5.8(b) shows a 30° dislocation formed by the dissociation of a 60° dislocation into a pair of partial dislocations that terminate either end of an intrinsic stacking fault.

The unpaired atomic columns at dislocation cores located at the interfacial plane, as visible in figs. 5.5, 5.7, and 5.8(b), were all composed primarily of either group III or V atoms, depending on the imaging orientation. At the ZnTe/InP and ZnTe/InAs interfaces, the unpaired atomic column consisted primarily of In atoms. The ZnTe/GaAs

interface was imaged along an orthogonal {110}-type zone axis, and the unpaired atomic column at this interface then consisted primarily of As atoms. These results are consistent with a previous study on 60° dislocations in GaAs/GaAsSb/GaAs heterostructures.[12]

5.5 Lomer Dislocations

Lomer dislocations were also identified at the ZnTe/InP ($\Delta a/a \sim 3.85\%$) and ZnTe/GaAs interfaces ($\Delta a/a \sim 7.4\%$), but were not seen at the ZnTe/InAs interface ($\Delta a/a \sim 0.74\%$).[17,20,25,26] A Lomer dislocation at the ZnTe/InP interface is shown in fig. 5.9, together with integrated intensity profiles measured at the locations shown in fig. 5.9(b). The intensity profile measured well away from the dislocation core, shown in fig. 5.9(d), indicates much greater P and Te intermixing compared to In and Zn, which appear to

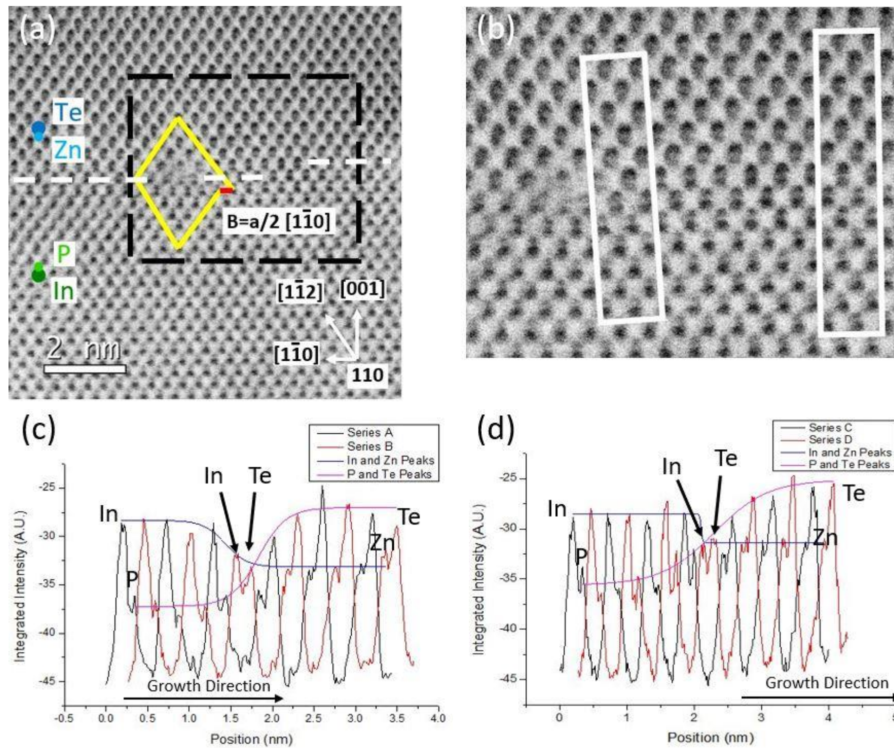

Figure 5.9: a) LABF STEM image of 90° dislocation core at ZnTe/InP (001) interface. The black, dashed rectangle indicates the region shown enlarged in (b). White rectangles indicate locations where intensity profiles were measured. c-d) Inverted integrated intensity profiles collected from (c) the left, and (d) the right, of (b).

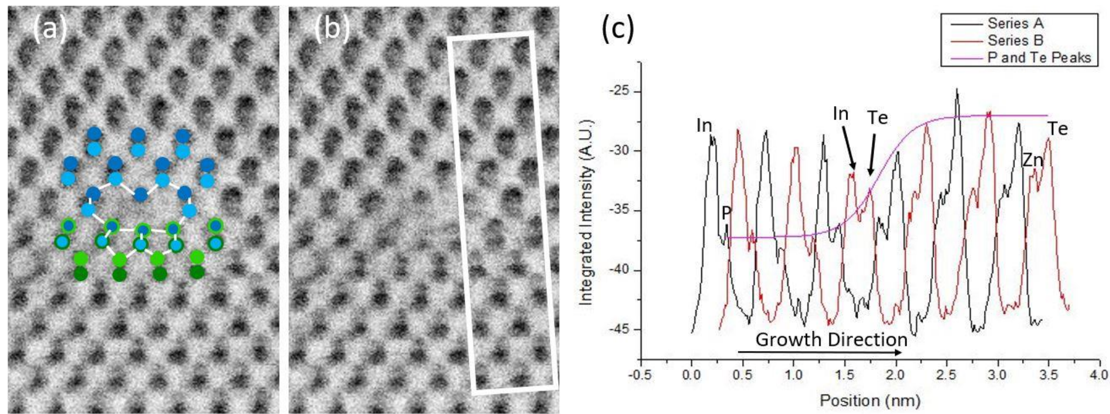

Figure 5.10: a) Proposed dislocation core structure superimposed on enlarged view of dislocation in figure 5.9(a). Atomic columns composed of Te, Zn, P, and In are marked with dark blue, light blue, light green, and dark green dots, respectively. The interfacial plane is marked with mixed blue and green dots for emphasis. b) Location where intensity profiles were measured marked with white rectangle. c) Inverted integrated intensity profile. Nominal interfacial plane, composed primarily of In and Te atomic columns, marked with arrows.

form an atomically abrupt transition. In contrast, the P-Te transition near the dislocation core, shown in fig. 5.9(c), is less extensive and suggests a broader In-Zn interfacial width. Careful comparison of figs. 5.9(c) and 5.9(d) also reveals that there is a step in the nominal interfacial plane to the right of the dislocation core. Approximate locations of the interfacial plane are shown with dashed white lines in fig. 5.9(a).

A proposed atomic structure for the dislocation core in fig. 5.9 is shown in fig. 5.10(a). The dislocation core is located just above the nominal interfacial plane, marked by arrows in the intensity profile shown in fig. 5.10(c). A 10-atom ring is located in the ZnTe layer just above the transitional atomic column pairs, while two 5-atom rings stretch across the interfacial plane. The location of the dislocation core corresponds well with the P-Te transition shown in fig. 5.10(c), which is also shifted slightly up into the ZnTe layer. This structure is very similar to the proposed structure of a Lomer dislocation at an InGaAs/GaAs interface.[13] Although the InGaAs/GaAs system does not have the

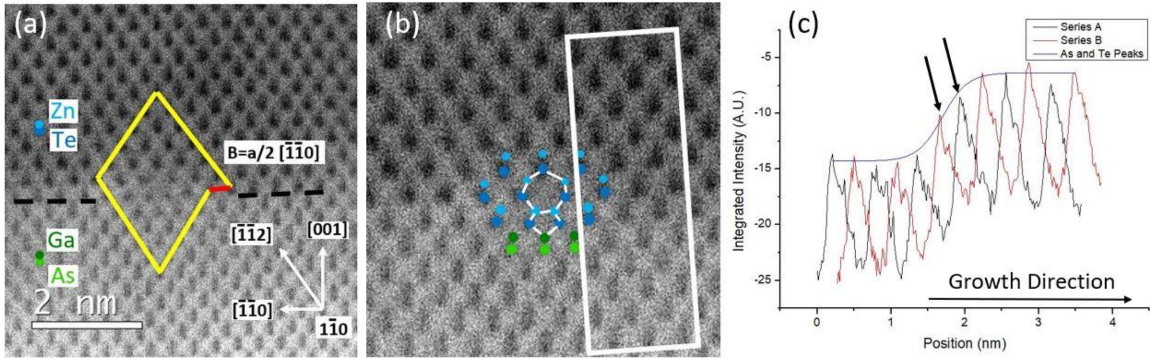

Figure 5.11: a) LABF STEM image of a conventional shuffle type Lomer dislocation at a ZnTe/GaAs (001) interface. b) Structural model of the dislocation core superimposed on an enlarged view of the core. c) Inverted integrated intensity profile taken from the region marked by the white rectangle in b.

same valence mismatch as the ZnTe/InP interface, the structures of the dislocation cores are in good agreement.

A conventional shuffle-type Lomer dislocation at the ZnTe/GaAs interface is shown in fig. 5.11. Intensity profiles measured near the dislocation core reveal that the interface is again not atomically abrupt. The dislocation core is comprised of transitional atomic columns that are likely dominated by Zn and Te atoms. A possible atomic-structure model for this type of defect, based on both the AC-STEM images and intensity profile data, is shown in fig. 5.11(b), with the approximate location of atomic columns marked by light blue, dark blue, dark green, and light green dots representing Zn, Te, Ga, and As columns, respectively. The locations of the 5- and 7-member rings of the dislocation core are marked by arrows in the integrated intensity profile in fig. 5.11(c). However, the chemical profile across the interface is not atomically abrupt, so that the atomic columns along the interface, particularly at the dislocation core, are not likely to consist of single atomic species.

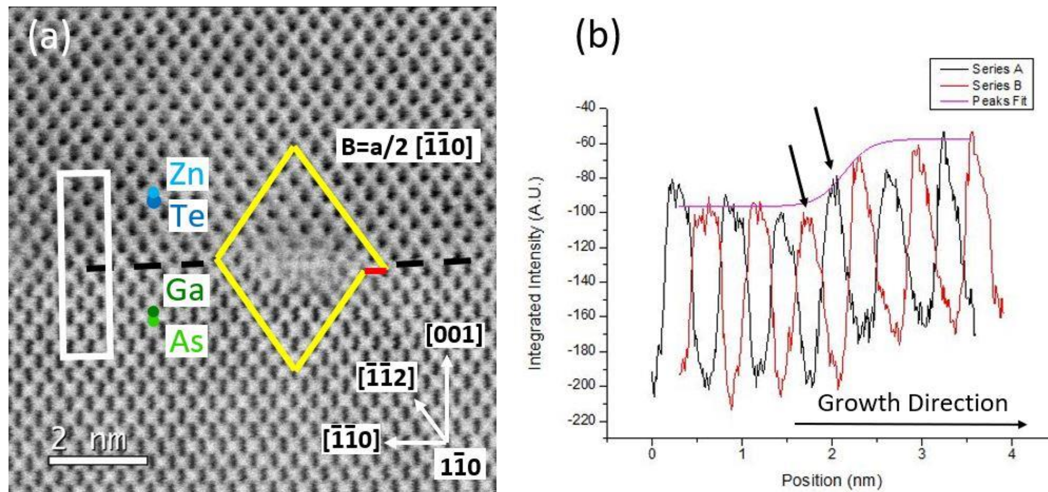

Figure 5.12: a) LABF STEM image of a Lomer dislocation at a ZnTe/GaAs (001) interface with a disordered core. b) Inverted integrated intensity profile measured from location marked with the white rectangle.

Lomer dislocations with disordered core structures, such as that shown in fig. 5.12(a), were more common along the ZnTe/GaAs interface. While the exact atomic structures of these dislocation cores are unclear, intensity profiles taken from near these disordered dislocations indicate that the cores are located at the lower transitional planes of the interface, as shown by the arrows in fig. 5.12(b), which is in contrast to the location of the MD core shown in fig. 5.11.

5.6 Discussion & Conclusions

This study has confirmed that heterovalent ZnTe/GaAs, ZnTe/InP and ZnTe/InAs II-VI/III-V (001) interfaces are not atomically abrupt, which complicates determination of the atomic structure of MD cores. The structural defects observed at the ZnTe/InAs interface ($\Delta a/a \sim 0.74\%$) are primarily 60° dislocations belonging to the glide set, which are located above the interface in the ZnTe layer. However, 30° partial dislocations formed through the dissociation of 60° dislocations were identified at the interfacial plane, and the individual, unpaired atomic column at these interfacial dislocation cores

contained mostly In atoms. 60° dislocations are located at the nominal interfacial plane for ZnTe/GaAs and ZnTe/InP (001) interfaces and correspond to a transition from II-V to III-VI bonding along the interfaces.

Previous workers have studied misfit dislocations at II-VI/III-V interfaces, but it was commonly observed that the dislocation cores seemed to be blurred compared to the surrounding lattice.[20,25,26] It has been suggested that this blurring could be partly due to sample preparation artefacts or beam-specimen interaction during TEM analysis. Results from this current study suggest that another reason for this blurring could be disorder along the dislocation line caused by intermixing across the heterovalent interface.

Overall, these results suggest that there is a correlation between misfit dislocation core structure and chemical intermixing at II-VI/III-V interfaces. Lomer dislocations are clearly more efficient at relaxing misfit strain due to lattice mismatch across heterovalent interfaces, whereas 60° dislocations may be more effective at accommodating valence mismatch. Intermixing across heterovalent interfaces is likely to be encouraged by the increased strain field at the dislocation cores, resulting in greater disorder along dislocation lines, particularly in comparison to similar dislocations at isovalent interfaces. Elemental mapping with electron-energy-loss spectroscopy measured simultaneously with AC-STEM imaging may help shed further light on the chemical composition of atomic columns at the dislocation cores.

References

[1] Z. I. Alferov, "The history and future of semiconductor heterostructures." Semiconductors, **32**, 1-14 (1998).

[2] J. Hornstra, "Dislocations in the diamond lattice." J. Phys. Chem. Solids, **5**, 129-141 (1958).

[3] C. Wen, "The Relationship Between Atomic Structure and Strain Distribution of Misfit Dislocation Cores at Cubic Heteroepitaxial Interfaces." Microsc. Microanal., **23**, 449-459 (2017).

[4] C. Wen and Y. J. Ma, "Determination of atomic-scale chemical composition at semiconductor heteroepitaxial interfaces by high-resolution transmission electron microscopy." Micron, **106**, 48-58 (2018).

[5] T. J. Gosling, "Mechanism for the formation of 90° dislocations in high-mismatch (100) semiconductor strained-layer systems." J. Appl. Phys., **74**, 5415–5420 (1993).

[6] D. J. Smith, "Atomic-scale characterization of II-VI compound semiconductors." J. Electron Mater., **42**, 3168–3174 (2013).

[7] W. Qian, M. Skowronski, R. Kaspi, M. De Graef, and V. P. Dravid, "Nucleation of misfit and threading dislocations during epitaxial growth of GaSb on GaAs (001) substrates." J. Appl. Phys., **81**, 7268-7272 (1997).

[8] S. H. Huang, G. Balakrishnan, A. Khoshakhlagh, A. Jallipalli, L. R. Dawson, and D. L. Huffaker, "Strain relief by periodic misfit arrays for low defect density GaSb on GaAs." Appl. Phys. Lett., **88**, 131911 (2006).

[9] Y. Wang, P. Ruterana, S. Kret, S. El Kazzi, L. Desplanque, and X. Wallart, "The source of the threading dislocation in GaSb/GaAs hetero-structures and their propagation mechanism." Appl. Phys. Lett., **102**, 052102 (2013).

[10] Y. Wang, P. Ruterana, J. Chen, S. Kret, S. El Kazzi, C. Genevois, L. Desplanque, and X. Wallart, "Antimony-mediated control of misfit dislocations and strain at the highly lattice mismatched GaSb/GaAs interface." ACS Appl. Mater. Interfaces, **5**, 9760-9764 (2013).

[11] J.N. Stirman, P.A. Crozier, D.J. Smith, F. Phillipp, G. Brill, and S. Sivananthan, "Atomic-scale imaging of asymmetric Lomer dislocation cores at the Ge/Si(001) heterointerface." Appl. Phys. Lett., **84**, 2530-2532 (2004).

[12] A. Gangopadhyay, A. Maros, N. Faleev, and D. J. Smith, "Atomic structure of dissociated 60° dislocations in GaAs/$GaAs_{0.92}Sb_{0.08}$/GaAs heterostructures." Scripta Mater., **153**, 77-80 (2018).

[13] K. Tillman, L. Houben, A. Thust, and K. Urban, "Spherical-aberration correction in tandem with the restoration of the exit-plane wavefunction: synergetic tools for the imaging of lattice imperfections in crystalline solids at atomic resolution." J. Mater. Sci., **41**, 4420-4430 (2006).

[14] N. Otsuka, C. Choi, Y. Nakamura, S. Nagakura, R. Fischer, C. K. Peng, and H. Morkoç, "High resolution electron microscopy of misfit dislocations in the GaAs/Si epitaxial interface." Appl. Phys. Lett., **49**, 277-279 (1986).

[15] S. Lopatin, S. J. Pennycook, J. Narayan, and G. Duscher, "Z-contrast imaging of dislocation cores at the GaAs/Si interface." Appl. Phys. Lett., **81**, 2728-2730 (2002).

[16] J. Narayan and S. Oktyabrsky, "Formation of misfit dislocations in thin film heterostructures." J. Appl. Phys., **92**, 7122-7127 (2002).

[17] L. Ouyang, J. Fan, S. Wang, X. Lu, Y. H. Zhang, X. Liu, J. K. Furdyna, and D. J. Smith, "Microstructural characterization of thick ZnTe epilayers grown on GaSb, InAs, InP and GaAs (1 0 0) substrates." J. Cryst. Growth, **330**, 30-34 (2011).

[18] J. K. Furdyna, and J. Kossut, "A simple lattice-matching guide for superlattices and heterostructures of tetrahedrally-bonded semiconductors." Superlattices and Microstructures, **2**, 89-96 (1986).

[19] Y. H. Zhang, S. N. Wu, D. Ding, S. Q. Yu, and S. R. Johnson, in *33rd. IEEE PVSC, 2008*, pp. 1-5.

[20] D. J. Smith, T. Aoki, J. K. Furdyna, X. Liu, M. R. McCartney, and Y. H. Zhang, "Atomic-scale characterization of (mostly zincblende) compound semiconductor heterostructures." *J. Phys.: Conf. Ser.* **471**, 012005 (2013).

[21] B. G. Streetman and S. Banerjee, *Solid State Electronic Devices* (5th ed.). New Jersey: Prentice Hall, 2000, p. 524.

[22] W. A. Harrison, E. A. Kraut, J. R. Waldrop, and R. W. Grant, "Polar heterojunction interfaces." Physical Review B, **18**, 4402-4410 (1978).

[23] Q. Liu, X. Zhang, L. B. Abdalla, and A. Zunger, "Transforming common III-V and II-VI semiconductor compounds into topological heterostructures: the case of CdTe/InSb superlattices." Adv. Funct. Mater., **26**, 3259-3267 (2016).

[24] S. Bauer, A. Rosenauer, J. Skorsetz, W. Kuhn, H. P. Wagner, J. Zweck, and W. Gebhardt, "Investigation of strained ZnTe epilayers by high resolution electron microscopy." J. Cryst. Growth, **117**, 297-302 (1992).

[25] D. J. Smith, T. Aoki, J. Mardinly, L. Zhou, and M. R. McCartney, "Exploring aberration-corrected electron microscopy for compound semiconductors." Microscopy, **62**, S65-S73 (2013).

[26] D. J. Smith, J. Lu, T. Aoki, M. R. McCartney, and Y. H. Zhang, "Observation of compound semiconductors and heterovalent interfaces using aberration-corrected scanning transmission electron microscopy." J. Mater. Res., **32**, 921-927 (2017).

[27] A. J. McGibbon, S. J. Pennycook, and J. E. Angelo, "Direct observation of dislocation core structures in CdTe/GaAs (001)." Science, **269**, 519-521 (1995).

[28] T. W. Kim, D. U. Lee, H. S. Lee, J. Lee, and H. L. Park, "Strain effects and atomic arrangements of 60° and 90° dislocations near the ZnTe/GaAs heterointerface." Appl. Phys. Lett., **78**, 1409-1411 (2001).

[29] S. Bauer, A. Rosenauer, P. Link, W. Kuhn, J. Zweck, and W. Gebhardt, "Misfit dislocations in epitaxial ZnTe/GaAs (001) studied by HRTEM." Ultramicroscopy, **51**, 221-227 (1993).

[30] J. Gao, W. Jie, Y. Yuan, T. Wang, Y. Xie, Y. Wang, Y. Huang, J. Tong, H. Yu, and G. Pan, "One-step fast deposition of thick epitaxial CdZnTe film on (001) GaAs by close-spaced sublimation." Cryst. Eng. Comm., **14**, 1790-1794 (2012).

CHAPTER 6

SUMMARY AND POSSIBLE FUTURE WORK

This dissertation has described the application of transmission electron microscopy (TEM) and aberration-corrected scanning TEM (AC-STEM) to characterize the atomic-scale structure of individual defects and defect clusters in compound semiconductor materials and devices. These studies were part of ongoing efforts to bridge the current knowledge gap between defect characterization and device performance at the atomistic scale. This chapter summarizes the major results of this work and briefly highlights possible opportunities for further investigation.

6.1 Summary

An extensive effort was made to identify specific locations of crystal defects in CdTe epilayers that might be shown to contribute to degraded light-conversion efficiency. Electroluminescence (EL) mapping and the creation of surface etch pits through chemical treatment were used in attempts to identify specific structural defects for subsequent TEM examination. However, a major obstacle impeding useful progress proved to be the experimental difficulty of identifying etch pits for study that corresponded to locations of decreased optical and electrical activity, as shown by EL mapping, and were of a suitable size, i.e., not so shallow as to be indistinguishable from the surrounding roughened surface but not so deep that the defect of interest had been completely removed by the etching process. The TEM studies of these specimens only revealed surface etch pits, and there was no visible sign of any extended defects at their base. It was also concluded that while the formation of etch pits could be helpful for

precisely locating extended defects associated with decreased optoelectrical activity, the surface roughness surrounding etch pits would tend to mitigate against their usefulness.

Defective regions in GaAs solar-cell devices were identified using combinations of photoluminescence (PL), EL, and Raman scattering, and these were then extracted for TEM analysis. It was observed that device degradation was invariably associated with a cluster of extended defects (EDs), rather than by a single ED, as had been previously assumed. Each defect cluster was found to be unique, while still sharing common characteristics. Careful comparison of the different defect clusters showed that every cluster was dominated by a collection of extended {111}-type stacking faults mostly located near the top of the device in the GaAs emitter and absorber layers. However, one defect cluster, with relatively short stacking faults, was primarily confined to the uppermost GaAs emitter layer, leaving the GaInP window layer free of defects, and the cluster only extended downwards into the GaAs absorber layer over a relatively short distance (~0.25 μm). Other defect clusters analyzed in these studies extended from the top of the device, originating in the GaInP window layer, through the GaAs emitter layer, and deep into the GaAs absorber layer; about 1-μm deep in one case and around 2.5-μm deep in another.

Atomic-scale arrangements of the defect clusters in these GaAs devices were investigated using aberration-corrected STEM. Individual defects in each cluster consisted primarily of an intrinsic stacking fault terminated by 30° and 90° partial dislocations. In some cases, sufficient structural resolution was achieved to identify the chemical species of individual atomic columns at the cores of the 30° partial dislocations. No unpaired atomic columns were, however, identified at the cores of the 90° partial

dislocations. Although these stacking faults and associated partial dislocations tended to dominate each defect cluster, 60° perfect dislocations and Lomer dislocations were also identified. For example, Lomer dislocations were identified near locations where two lines of strain contrast intersected in a large defect cluster adjacent to a surface pit. Other defect clusters exhibited far fewer of these intersections and no Lomer dislocations were identified in those clusters. A comparatively shallow cluster, largely constrained to the GaAs emitter layer, contained 60° perfect dislocations associated with localized strain contrast, but did not seem associated with any stacking faults. No 60° perfect dislocations were seen in two other clusters, which were dominated by long stacking faults.

In another study, it was confirmed that heterovalent ZnTe/GaAs, ZnTe/InP and ZnTe/InAs II-VI/III-V (001) interfaces are not atomically abrupt, which complicates determination of the atomic structure of MD cores. It was suggested that a reason for blurred MD cores at II-VI/III-V interfaces could be disorder along the dislocation line caused by intermixing across the heterovalent interface. The structural defects observed at the ZnTe/InAs interface ($\Delta a/a \sim 0.74\%$) were primarily 60° dislocations belonging to the glide set, which were located above the interface in the ZnTe layer. However, 30° partial dislocations formed through the dissociation of 60° dislocations were identified at the interfacial plane, and the individual, unpaired atomic column at these interfacial dislocation cores contained mostly In atoms. 60° dislocations were located at the nominal interfacial plane for ZnTe/GaAs and ZnTe/InP (001) interfaces and correspond to a transition from II-V to III-VI bonding along the interfaces.

Overall, these results suggest that there is a correlation between misfit dislocation core structure and chemical intermixing at II-VI/III-V interfaces. Lomer dislocations are clearly more efficient at relaxing misfit strain due to lattice mismatch across heterovalent interfaces, whereas 60° dislocations may be more effective at accommodating valence mismatch. Intermixing across heterovalent interfaces is likely to be encouraged by the increased strain field at the dislocation cores, resulting in greater disorder along dislocation lines, particularly in comparison to similar dislocations at isovalent interfaces.

6.2 Possible Future Work

Damage to a specimen that is introduced during the process of sample preparation has been an ongoing issue for many years, especially for semiconductor materials, and continues to complicate reliable TEM analysis.[2,3] Work is constantly underway to find alternative methods for preparing TEM specimens faster, and more reliably, but with less artefactual damage. For example, it has been shown that different ion-beam sources in focused ion-beam (FIB) systems produce dramatically different results with regard to milling rate, ion implantation, and surface amorphization during TEM sample preparation.[4,5] Frequently, ion-beam sources result in reduced specimen damage, but they also correspond to greatly reduced milling rates. If FIB systems incorporated several different ion-beam sources, then they could be used in series to incrementally thin materials to electron transparency, using the fastest and most damaging ions first and then progressing to ions that remove material more slowly and with minimal sample damage. Future studies involving semiconductor materials, particularly III-V and II-VI materials which were once again confirmed to be susceptible to ion-beam damage during the

investigations described in this dissertation, would benefit from the use of FIB systems equipped with multiple ion-beam sources to improve these prospects.

In this dissertation research, it was shown that chemically etching CdTe was ineffective for reliably identifying defect locations for later TEM investigation. Previous work had also concluded that not all chemical etch pits corresponded to potential defect sites revealed by PL imaging or *vice versa*.[6] Thus, if the primary interest is to correlate specific structural defects with locally degraded performance then a different approach for locating and characterizing individual optoelectrically active defects in CdTe is highly desirable. It was demonstrated that optoelectrically active defects in GaAs solar-cell devices could be precisely located using PL and/or EL imaging without damaging the device surface. A similar study of defect structures in CdTe epilayers should be carried out where PL and EL imaging are used to identify possible defect locations, rather than the use of any chemical etching. Thus, a study in which optoelectrically active defects are located through the use of EL mapping, or similar techniques, and their locations precisely measured relative to recognizable surface features, should result in a higher percentage of extended defects being successfully isolated for TEM characterization and correlation with device properties. Alternatively, reasons explaining why EL dark spots and the locations of surface etch pits did not generally correspond to each other could be more effectively investigated by selecting a material system where chemical etching was less destructive to non-defective material relative to defect sites.

References

[1] L. Ouyang, J. Fan, S. Wang, X. Lu, Y.-H. Zhang, X. Liu, J. K. Furdyna, and D. J. Smith, "Microstructural characterization of thick ZnTe epilayers grown on GaSb, InAs, InP, and GaAs (1 0 0) substrates." J. Cryst. Growth, **330**, 30-34 (2011).

[2] Á. Barna, B. Pécz, and M. Menyhard, "TEM sample preparation by ion milling/amorphization." Micron, **30**, 267-276 (1999).

[3] J. Belz, A. Beyer, T. Torunski, W. Stolz, and K. Volz, "Direct investigation of (sub-) surface preparation artifacts in GaAs based materials by FIB sectioning." Ultramicroscopy **163**, 19-30 (2016).

[4] L. Bischoff, P. Mazarov, L. Bruchhaus, and J. Gierak, "Liquid metal alloy ion sources– An alternative for focused ion beam technology." Applied Physics Reviews, **3**, 021101 (2016).

[5] B. Knuffman, A. V. Steele, and J. J. McClelland, "Cold atomic beam ion source for focused ion beam applications." J. Appl. Phys., **114**, 044303 (2013).

[6] H. Liu, Y. Zhang, Y. Chen, and P. S. Wijewarnasuriya, "Confocal Micro-PL Mapping of Defects in CdTe Epilayers Grown on Si (211) Substrates with Different Annealing Cycles." J. Elec. Materi., **43**, 2854 (2014).

REFERENCES

Á. Barna, B. Pécz, and M. Menyhard, “TEM sample preparation by ion milling/amorphization.” Micron, **30**, 267-276 (1999).

A. Gangopadhyay, A. Maros, N. Faleev, and D. J. Smith, “Atomic structure of dissociated 60° dislocations in GaAs/$GaAs_{0.92}Sb_{0.08}$/GaAs heterostructures.” Scripta Mater., **153**, 77-80 (2018).

A. J. McGibbon, S. J. Pennycook, and J. E. Angelo, “Direct observation of dislocation core structures in CdTe/GaAs (001).” Science, **269**, 519-521 (1995).

B. Fultz and J. Howe, Transmission Electron Microscopy and Diffractometry of Materials, Springer-Verlag, Berlin Heidelberg, 2013.

B. G. Streetman and S. Banerjee, *Solid State Electronic Devices* (5th ed.). New Jersey: Prentice Hall, 2000, p. 524.

B. Knuffman, A. V. Steele, and J. J. McClelland, “Cold atomic beam ion source for focused ion beam applications.” J. Appl. Phys., **114**, 044303 (2013).

B. Van Zeghbroeck, Principles of Semiconductor Devices, ECEE Colorado, 2011.

C. Kittel, Introduction to Solid State Physics. John Wiley & Sons, Incorporated, 2005.

C. Li, J. Poplawsky, Y. Yan, and S. J. Pennycook, “Understanding individual defects in CdTe thin-film solar cells via STEM: From atomic structure to electrical activity.” Materials Science in Semiconductor Processing, **65**, 64-76 (2017).

C. S. Ferekides, D. Marinskiy, V. Viswanathan, B. Tetali, V. Palekis, P. Selvaraj, and D. L. Morel, "High efficiency CSS CdTe solar cells." Thin Solid Films, **361**, 520-526 (2000).

C. Wen and Y. J. Ma, “Determination of atomic-scale chemical composition at semiconductor heteroepitaxial interfaces by high-resolution transmission electron microscopy.” Micron, **106**, 48-58 (2018).

C. Wen, "The Relationship Between Atomic Structure and Strain Distribution of Misfit Dislocation Cores at Cubic Heteroepitaxial Interfaces." Microsc. Microanal., **23**, 449-459 (2017).

Cheung, N. (2020, February 13). Defects Tutorial. Retrieved from http://www-inst.eecs.berkeley.edu/~ee143/sp06/lectures/Defects_tutorial.pdf

D. A. Cullen and D. J. Smith, “Assessment of surface damage and sidewall implantation in AlGaN-based high electron mobility transistor devices caused during focused-ion-beam milling.” J. Appl. Phys., **104**, 094304 (2008).

D. A. Cullen, D. J. Smith, A. Passaseo, V. Tasco, A. Stocco, M. Meneghini, G. Meneghesso, and E. Zanoni, "Electroluminescence and Transmission Electron Microscopy Characterization of Reverse-Biased AlGaN/GaN Devices." IEEE Transactions on Device and Materials Reliability, **13**, 126-135 (2013).

D. B. Williams and C. B. Carter, Transmission Electron Microscopy: A Textbook for Materials Science, Second Edition. Springer, New York, 2009, p. 5.

D. B. Williams op. cit. p. 11.

D. B. Williams op. cit. p. 26.

D. B. Williams op. cit. p. 86.

D. B. Williams op. cit. p. 98.

D. B. Williams op. cit. pp. 177-182.

D. B. Williams op. cit. pp. 372-389.

D. B. Williams op. cit. pp. 597, 663-665.

D. J. Smith, "Atomic-scale characterization of II-VI compound semiconductors." J. Electron Mater., **42**, 3168–3174 (2013).

D. J. Smith, "Development of aberration-corrected electron microscopy." Microsc. Microanal. **14**, 2–15 (2008).

D. J. Smith, J. Lu, T. Aoki, M. R. McCartney, and Y. H. Zhang, "Observation of compound semiconductors and heterovalent interfaces using aberration-corrected scanning transmission electron microscopy." J. Mater. Res., **32**, 921-927 (2017).

D. J. Smith, T. Aoki, J. K. Furdyna, X. Liu, M. R. McCartney, and Y. H. Zhang, "Atomic-scale characterization of (mostly zincblende) compound semiconductor heterostructures." *J. Phys.: Conf. Ser.* **471**, 012005 (2013).

D. J. Smith, T. Aoki, J. Mardinly, L. Zhou, and M. R. McCartney, "Exploring aberration-corrected electron microscopy for compound semiconductors." Microscopy, **62**, S65-S73 (2013).

G. Salviati, M. Albrecht, C. Zanotti-Fregonara, N. Armani, M. Mayer, Y. Shreter, M. Guzzi, Yu. V. Melni, K. Vassilevski, V. A. Dmitriev, and H. P. Strunk, "Cathodoluminescence and transmission electron microscopy study of the influence of crystal defects on optical transitions in GaN." Physica Status Solidi (a), **171**, 325-339 (1999).

H. K. Henisch, Electroluminescence. In: H. K. Henisch, International Series of Monographs on Semiconductors Volume 5. Pergamon Press, 1962, pp. 5-6.

H. K. Henisch op. cit. pp. 6-7, 41, 94-104.

H. K. Henisch op. cit. pp. 40, 94-96.

H. K. Henisch op. cit. pp. 96-104.

H. K. Henisch op. cit. pp. 104-107.

H. Liu, Y. Zhang, Y. Chen, and P. S. Wijewarnasuriya, "Confocal Micro-PL Mapping of Defects in CdTe Epilayers Grown on Si (211) Substrates with Different Annealing Cycles." J. Elec. Materi., **43**, 2854 (2014).

J. Belz, A. Beyer, T. Torunski, W. Stolz, and K. Volz, "Direct investigation of (sub-) surface preparation artifacts in GaAs-based materials by FIB sectioning." Ultramicroscopy, **163**, 19-30 (2016).

J. Gao, W. Jie, Y. Yuan, T. Wang, Y. Xie, Y. Wang, Y. Huang, J. Tong, H. Yu, and G. Pan, "One-step fast deposition of thick epitaxial CdZnTe film on (001) GaAs by close-spaced sublimation." Cryst. Eng. Comm., **14**, 1790-1794 (2012).

J. Hornstra, "Dislocations in the diamond lattice." J. Phys. Chem. Solids, **5**, 129-141 (1958).

J. I. Goldstein, D. E. Newbury, J. R. Michael, N. W. M. Ritchie, J. H. J. Scott and D. C. Joy, Scanning Electron Microscopy and X-Ray Microanalysis. Springer, 2003, pp. 22-24.

J. I. Goldstein op. cit. p. 2.

J. I. Goldstein op. cit. pp. 40-42.

J. I. Goldstein op. cit. pp. 195-197.

J. K. Furdyna, and J. Kossut, "A simple lattice-matching guide for superlattices and heterostructures of tetrahedrally-bonded semiconductors." Superlattices and Microstructures, **2**, 89-96 (1986).

J. L. Crozier, E. E. van Dyk and F. J. Vorster, "High Resolution Spatial Electroluminescence Imaging of Photovoltaic Modules." Vor. Nelson Mand. Metrop. Univ. (2009).

J. L. Weyher, In The Encyclopedia of Advanced Materials "Compound Semiconductors: Defects Revealed by Etching." ed. D. Bloor, R. J. Brook, M. C. Flemings, and S. Mahajan. Oxford: Pergamon Press, 1994, p. 460.

J. Narayan and S. Oktyabrsky, “Formation of misfit dislocations in thin film heterostructures.” J. Appl. Phys., **92**, 7122-7127 (2002).

J. S. Blakemore, “Semiconducting and other major properties of gallium arsenide.” J. Appl. Phys., **53**, (1982).

J. Y. Dai, S. F. Tee, C. L. Tay, Z. G. Song, S. Ansari, E. Er, and S. Redkar, “Development of a rapid and automated TEM sample preparation method in semiconductor failure analysis and the study of the relevant TEM artifact.” Microelectronics Journal, **32**, 221-226 (2001).

J. N. Stirman, P. A. Crozier, D. J. Smith, F. Phillipp, G. Brill, and S. Sivananthan, “Atomic-scale imaging of asymmetric Lomer dislocation cores at the Ge/Si(001) heterointerface.” Appl. Phys. Lett., **84**, 2530-2532 (2004).

K. Tillman, L. Houben, A. Thust, and K. Urban, “Spherical-aberration correction in tandem with the restoration of the exit-plane wavefunction: synergetic tools for the imaging of lattice imperfections in crystalline solids at atomic resolution.” J. Mater. Sci., **41**, 4420-4430 (2006).

L. Bischoff, P. Mazarov, L. Bruchhaus, and J. Gierak, “Liquid metal alloy ion sources–An alternative for focused ion beam technology.” Appl. Phys. Rev., **3**, 021101 (2016).

L. M. Woods, D. H. Levi, V. Kaydanov, G. Y. Robinson, and R. K. Ahrenkiel, "Electrical characterization of etched grain-boundary properties from as-processed px-CdTe-based solar cells." In AIP Conference Proceedings, **462**, 499-504. American Institute of Physics, (1999).

L. Ouyang, J. Fan, S. Wang, X. Lu, Y. H. Zhang, X. Liu, J. K. Furdyna, and D. J. Smith, “Microstructural characterization of thick ZnTe epilayers grown on GaSb, InAs, InP and GaAs (1 0 0) substrates.” J. Cryst. Growth, **330**, 30-34 (2011).

M. A. Green, K. Emery, Y. Hishikawa, W. Warta, and E. D. Dunlop, “Solar cell efficiency tables (version 46).” Prog. Photovolt.: Res. Appl., **23**, 805-812 (2015).

M. A. O'Keefe, L. F. Allard, and D. A. Blom, “HRTEM imaging of atoms at sub-Ångström resolution.” J. Electron Microsc., **54**, 169-180 (2005).

M. Fukuda, “Historical overview and future of optoelectronics reliability for optical fiber communication systems.” Microelectronics Reliability **40**, 27-35 (2000).

M. H. F. Overwijk, F. C. Van den Heuvel, and C. W. T. Bulle-Lieuwma, “Novel scheme for the preparation of transmission electron microscopy specimens with a focused ion beam.” Journal of Vacuum Science & Technology B: Microelectronics and Nanometer Structures Processing, Measurement, and Phenomena, **11**, 2021-2024 (1993).

M. Vaghayenegar, K. J. Doyle, S. Trivedi, P. Wijewarnasuriya, and D. J. Smith, "Microstructural Characterization of Defects and Chemical Etching for HgCdSe/ZnTe/Si (211) Heterostructures." J. Elec. Materi., **48**, 571-582 (2018).

N. Otsuka, C. Choi, Y. Nakamura, S. Nagakura, R. Fischer, C. K. Peng, and H. Morkoç, "High resolution electron microscopy of misfit dislocations in the GaAs/Si epitaxial interface." Appl. Phys. Lett., **49**, 277-279 (1986).

O-S-D Report, IC Insights, (2017) http://www.icinsights.com/services/osd-report/report-contents/

P. V. Meyers, "Design of a thin film CdTe solar cell." Solar cells, **23**, 59-67 (1988).

Q. Chen, B. S. McKeon, J. Becker, S. Zhang, C.-K. Hu, T. H. Gfroerer, M. W. Wanlass, Y.-H. Zhang, D. J. Smith, and Y. Zhang, "Correlative characterization of dislocation defects and defect clusters in GaAs and CdTe solar cells by spatially resolved optical techniques and high-resolution TEM." 2018 IEEE 7th World Conference on Photovoltaic Energy Conversion (WCPEC), Waikoloa Village, HI, 2018, pp. 3234-3236.

Q. Liu, X. Zhang, L. B. Abdalla, and A. Zunger, "Transforming common III-V and II-VI semiconductor compounds into topological heterostructures: the case of CdTe/InSb superlattices." Adv. Funct. Mater., **26**, 3259-3267 (2016).

R. Erni, M. D. Rossell, C. Kisielowski, and U. Dahmen, "Atomic-Resolution Imaging with a Sub-50-pm Electron Probe." Phys. Rev. Lett. **102**, (2009).

R. J. D. Tilley, Defects in Solids. John Wiley & Sons, Incorporated, 2008, p. 85.

R. J. D. Tilley op. cit. pp. 8-9.

S. Bauer, A. Rosenauer, J. Skorsetz, W. Kuhn, H. P. Wagner, J. Zweck, and W. Gebhardt, "Investigation of strained ZnTe epilayers by high resolution electron microscopy." J. Cryst. Growth, **117**, 297-302 (1992).

S. Bauer, A. Rosenauer, P. Link, W. Kuhn, J. Zweck, and W. Gebhardt, "Misfit dislocations in epitaxial ZnTe/GaAs (001) studied by HRTEM." Ultramicroscopy, **51**, 221-227 (1993).

S. H. Huang, G. Balakrishnan, A. Khoshakhlagh, A. Jallipalli, L. R. Dawson, and D. L. Huffaker, "Strain relief by periodic misfit arrays for low defect density GaSb on GaAs." Appl. Phys. Lett., **88**, 131911 (2006).

S. J. Sweeney and J. Mukherjee, (2017) Optoelectronic Devices and Materials. In: Kasap S., Capper P. (eds) Springer Handbook of Electronic and Photonic Materials. Springer Handbooks. Springer, Cham.

S. Lopatin, S. J. Pennycook, J. Narayan, and G. Duscher, “Z-contrast imaging of dislocation cores at the GaAs/Si interface.” Appl. Phys. Lett., **81**, 2728-2730 (2002).

S. Mahajan and K. S. Sree Harsha, Principles of Growth and Processing of Semiconductors. McGraw-Hill, 1999, pp. 122-123.

S. Mahajan op. cit. pp. 123-128

S. Mahajan op. cit. pp. 26-34.

T. Aoki, J. Lu, M. R. McCartney, and D. J. Smith, “Bright-field imaging of compound semiconductors using aberration-corrected scanning transmission electron microscopy.” Semicond. Sci. Technol., **31**, (2016).

T. H. Gfroerer, Y. Zhang, and M. W. Wanlass, “An extended defect as a sensor for free carrier diffusion in a semiconductor.” Appl. Phys. Lett., **102**, 012114 (2013).

T. J. Gosling, “Mechanism for the formation of 90° dislocations in high-mismatch (100) semiconductor strained-layer systems.” J. Appl. Phys., **74**, 5415–5420 (1993).

T. W. Kim, D. U. Lee, H. S. Lee, J. Lee, and H. L. Park, “Strain effects and atomic arrangements of 60° and 90° dislocations near the ZnTe/GaAs heterointerface.” Appl. Phys. Lett., **78**, 1409-1411 (2001).

W. A. Harrison, E. A. Kraut, J. R. Waldrop, and R. W. Grant, “Polar heterojunction interfaces.” Physical Review B, **18**, 4402-4410 (1978).

W. Qian, M. Skowronski, R. Kaspi, M. De Graef, and V. P. Dravid, “Nucleation of misfit and threading dislocations during epitaxial growth of GaSb on GaAs (001) substrates.” J. Appl. Phys., **81**, 7268-7272 (1997).

Y. A. R. Dasilva, R. Kozak, R. Erni, and M. D. Rossell, “Structural defects in cubic semiconductors characterized by aberration-corrected scanning transmission electron microscopy.” Ultramicroscopy, **176**, 11-22 (2017).

Y. H. Zhang, S. N. Wu, D. Ding, S. Q. Yu, and S. R. Johnson, in 33rd. IEEE PVSC, 2008, pp. 1-5

Y. Wang, P. Ruterana, J. Chen, S. Kret, S. El Kazzi, C. Genevois, L. Desplanque, and X. Wallart, “Antimony-mediated control of misfit dislocations and strain at the highly lattice mismatched GaSb/GaAs interface.” ACS Appl. Mater. Interfaces, **5**, 9760-9764 (2013).

Y. Wang, P. Ruterana, S. Kret, S. El Kazzi, L. Desplanque, and X. Wallart, “The source of the threading dislocation in GaSb/GaAs hetero-structures and their propagation mechanism.” Appl. Phys. Lett., **102**, 052102 (2013).

Z. I. Alferov, “The history and future of semiconductor heterostructures.”
Semiconductors, **32**, 1-14 (1998).